UNIVERSITÀ DEGLI STUDI DI PALERMO
Dottorato di Ricerca in Ingegneria Elettrica, Elettronica e delle Telecomunicazioni, Matematica e Automatica
Dipartimento di Energia, ingegneria dell'Informazione e modelli Matematici
S.S.D.: ING-IND/32 , ING-INF/01

# WIRELESS CHARGING SYSTEMS FOR ELECTRIC VEHICLE BATTERIES

TESI DI DOTTORATO DI:
**ING. FILIPPO PELLITTERI**

COORDINATORE DEL CORSO DI DOTTORATO:
**PROF.SSA MARIA STELLA MONGIOVÌ**

TUTOR:
**PROF. ROSARIO MICELI**

CO-TUTOR:
**PROF. GIUSEPPE CAPPONI**

TUTOR NEL PERIODO ALL'ESTERO:
**PROF. UDAYA K. MADAWALA**

CICLO: XXVI
ANNO CONSEGUIMENTO TITOLO: 2016

UNIVERSITÀ DEGLI STUDI DI PALERMO
Dottorato di Ricerca in Ingegneria Elettrica, Elettronica e delle Telecomunicazioni,
Matematica e Automatica
Dipartimento di Energia, ingegneria dell'Informazione e modelli Matematici
S.S.D.: ING-IND/32 , ING-INF/01

# WIRELESS CHARGING SYSTEMS FOR ELECTRIC VEHICLE BATTERIES

TESI DI DOTTORATO DI:
**ING. FILIPPO PELLITTERI**
Filippo Pellitteri

IL DELEGATO AL
COORDINATORE DEL CORSO DI DOTTORATO:
**PROF.SSA MARIA STELLA MONGIOVÌ**

TUTOR:
**PROF. ROSARIO MICELI**
Rosario Miceli

CO-TUTOR:
**PROF. GIUSEPPE CAPPONI**
Giuseppe Capponi

TUTOR NEL PERIODO ALL'ESTERO:
**PROF. UDAYA K. MADAWALA**

CICLO: XXVI
ANNO CONSEGUIMENTO TITOLO: 2016

*Alla mia famiglia e a Chiara, loro sanno perché…*

# Acknowledgements

I would like to sincerely thank my PhD supervisors, Prof. Dr. Rosario Miceli, Prof. Dr. Giuseppe Capponi and Prof. Dr. Udaya K. Madawala.

I express my devoted gratitude to Prof. Dr. Rosario Miceli: his technical and human support throughout the three-year duration of my PhD course has been fundamental. I would like to thank him for the trust he always have put in me and for his great help to improve myself.

I offer my sincere thanks to Prof. Dr. Giuseppe Capponi for the background he gave me in the field of Electronics and for the kind help to my work.

I really thank Prof. Dr. Udaya K. Madawala for hosting me in the Power Electronics Laboratories of University of Auckland (New Zealand) during my three-month research period abroad. He has been fundamental to the development of the efficiency optimization algorithm that has been proposed in this thesis.

I would like to thank Dr. Valeria Boscaino for her theoretical support in the field of Power Electronics and for her precious help in the experimental tests.

I wish to express my gratitude to Dr. Antonino Oscar Di Tommaso for his theoretical support regarding the inductive coupling and for his fundamental contribution to build the coils that have been mounted on the prototype.

I express my appreciation to Prof. Dr. Guido Ala and Dr. Salvatore Ganci for their theoretical and practical help during the last part of my work, essential for the magnetic characterization of the prototype.

I would like to thank Dr. Massimo Caruso for his kindness, technical support and help every time I needed. He has been a precious co-worker throughout the last year of my PhD course.

I express my affectionate thanks to Dr. Andrea Puccio. He has been a PhD colleague of mine throughout all the three-year course. I wish to thank him for his constant presence and for his great help, and for being not only a colleague, but also a precious friend.

Last but not least, I would like to thank the University of Palermo for giving me great opportunities as researcher and man.

There are also some people I should write my thanks to, but I don’t need to: they already know.

# Contents

## Chapter I

## Chapter II

# Chapter III

# Introduction

The wireless solution is increasingly spreading as method of battery charging for Electric Vehicles (EVs). The standard technology of wireless EV battery charging is based on the Inductive Power Transfer (IPT) between two coupled coils, one connected to the electrical grid and the other one connected to the rechargeable battery. The IPT provides benefits in terms of safety and comfort, due to the absence of a plug-in operation: through IPT, the electrocution risk typically arising from power cords is avoided and the battery charging operation can automatically start.

According to the state of the EV, there are mainly two types of IPT for the wireless charging: static IPT, when the vehicle is stationary and nobody is inside it (e.g. in a parking area); dynamic or quasi-dynamic IPT, when the vehicle is being used (e.g. while in motion or during the traffic red light). The wireless power transfer obviously represents the only solution for the dynamic charging, since the wired connection would be impossible during the motion.

In spite of the undeniable advantages brought by Inductive Power Transfer, the researchers have to deal with several issues in order to make this technology even more attractive for the EV market.

First of all, an IPT system is inherently less efficient in terms of power transfer efficiency if compared to a conventional wire-based system. Indeed, due the magnetic coupling between the coils, there is an unavoidable minimum leakage magnetic field, leading to an energy loss. Furthermore, some technical aspects need to be taken into account in the practical implementation of an IPT system: for example, in order to obtain the maximum coupling, the misalignment between the coils must be as small as possible. As far as safety is concerned, even if the IPT allows to reduce the electrocution risk, some care is required regarding the magnetic field exposure.

In addition to design-related issues, other important considerations should be made, such as costs, infrastructural implications, standardization and customer reception.

The inductive coupling can be also exploited for a reverse power flow, that is from the vehicle to the grid. The Vehicle-to-grid (V2G) is a wide-spread concept, belonging to the up-to-date idea of the active demand: in a smart electrical network, the consumer is able to become producer of energy. The wireless power transfer can represent a support to V2G, and therefore be a Bi-Directional Inductive Power Transfer (BDIPT).

In Chapter I the main applications of wireless battery charging are addressed. All the possible power levels are considered, from the μW of Wireless Sensor Networks (WSN) to the hundreds of kW of Railway Applications, passing through the following applications: electric toothbrush, consumer electronic devices, household appliances and Electric Vehicles (EVs). A technical background on the IPT systems is provided, particularly focusing on the electronic and the magnetic design. After that, the IPT applied to EVs is discussed as far as general overview and state of the art are concerned: considerations on magnetic couplers, design methodologies, control strategies and safety issues are carried out. In the end, the main goals of the thesis are discussed.

In Chapter II an IPT system for wireless E-bike battery charging is proposed. Special care is taken towards the design of the coupled coils and of the power electronics system. A 36 V $LiFePO_4$ battery and an electrical power ranging from 100 W to 250 W are considered. Simulations have been carried out through *PowerSIM* software. Issues such as bifurcation and skin effect are addressed as well.

In addition to the system design, a typical Bi-Directional Inductive Power Transfer (BDIPT) system is deeply analyzed, in terms of power transfer and efficiency as function of specific control parameters, and an efficiency optimization algorithm is proposed. The mathematical analysis is validated through the electronic simulations.

In place of the designed and assembled inductive coils, alternative solutions of inductive coupling are proposed. All these solutions feature an air gap between the coils and are sized according to the dimensions of a bicycle wheel. An investigation on these options, carried out through the *COMSOL Multiphysics* software, leads to define the best solution in terms of efficiency and tolerance to misalignments. The comparison is made considering the accurate model of the whole system, including also the switching losses inside the electronic components.

In Chapter III the experimental results are presented. The laboratory prototype building is based on the designed system, featuring a coupling solution with flat and circular coils. Component sizing and PCB layout design are thoroughly discussed. In the end, the experimental results in terms of system working and power transfer efficiency are provided. A magnetic characterization of the prototype is given as well, aiming at the evaluation of the distance from the system at which the magnetic field exposure guidelines, provided by the International Commission on Non-Ionizing Radiation Protection (ICNIRP), are respected. The discussion about physiological compatibility of IPT systems is supported by magnetic simulations and measurements on the proposed system, for a 100 W power transfer.

# Chapter I

# Wireless battery charging for Electric Vehicles: introduction and state of the art

The wireless solution represents an ever-growing method of battery charging in several applications. The lack of wires is desirable whenever the power cable is inconvenient or even impossible to use. Wireless battery charging can be employed in different applications, ranging from the ultra-low power levels of the wireless sensors to the ultra-high power levels of the Railway Applications and passing through the following examples: electrical toothbrush [1], mobile phone [2], laptop [3], television [4], electric bicycle [5], electric car [6], electric bus [7].

## I.1. Wireless charging for low-power applications

The wireless battery charging for low-power devices ranges from ultra-low power applications, such as wireless sensors or implantable devices, to consumer electronic devices, such as smartphones or notebooks. The ultra-low power devices range from µW to mW power levels, whereas the power levels of the consumer electronic devices range from some W (e.g. mobile phones) to tens of W (e.g. laptops).

### I.1.1. Wireless Sensor Networks and biomedical applications

In Wireless Sensor Networks (WSN) the use of wires for the power supplying is generally impossible, since the wireless sensors are inherently hard to reach from the human beings, like in meteorological data collecting or military applications. In similar applications, the wireless solution represents the best option for both communications and power supplying. This application corresponds to ultra-low power levels, ranging from µW to mW.

In [8–10], the following method of wireless battery charging for nodes of a WSN is proposed: a wireless charging vehicle (WCV) travels along a planned path inside the network and recharges the sensors, through an inductive power transfer link. In [11] a power transfer inductive link is proposed to supply the batteries of the WSN nodes. The distance between the inductive coils is in the range (1÷10) mm.

The use of the environmental energy harvesting in order to supply the sensors can be considered as a form of wireless battery charging: in [12] and [13] the batteries and the supercapacitors of sensor nodes are respectively supplied by radio-frequency waves and solar power.

Wireless power transfer is also convenient in biomedical applications for the supply of implantable devices. In [14–18] several examples of wireless battery charging systems for implanted devices are proposed and investigated.

### I.1.2. Consumer electronic devices and household appliances

The following range of power levels is represented by the electronic consumer devices, such as mobile phones and notebooks. For these applications, the power level range from some W to tens of W. The wireless battery charging for mobile phones is fully commercialized and standardized [19].

This wireless charging is based on the Inductive Power Transfer (IPT) between two coupled coils: one of them is placed inside a pad and connected to the electrical grid, the other one is placed inside the device and connected to the electric battery. By positioning the mobile device upon the pad, the charging operation automatically starts through magnetic induction. A standard has been created by Wireless Power Consortium (WPC) to build a common platform that helps the compatibility between wireless charging stations and mobile devices. More than 200 companies have joined WPC [20].

One of the most attractive benefits brought by wireless battery charging for consumer electronics is the opportunity to simultaneously charge different devices on the same pad, as suggested by Fig. I.1 [21].

Fig. I.1. Commercial example of a wireless multi-charging station [21]

In [22] and [23] an innovative topology of power receiver of wireless battery charger for consumer devices is proposed.

As far as household appliances are concerned, [24] provides an example of an IPT system for a 1 kW power level, considerable as the peak power for the low-power range.

## I.2. Wireless charging for Electric Vehicles

If compared to the consumer electronic devices, the electric vehicles (EV) charging occurs at notably higher power levels, ranging from a few hundreds of W (as in the case of the E-bike) to several tens of kW (as in the case of the electric buses). The Wireless Electric Vehicle Charging (WEVC) is still far from a full commercialization and standardization. Nevertheless, being implemented through Inductive Power Transfer (IPT) between two coupled coils, it provides benefits in terms of safety and comfort to all the users.

The EVs can be recharged or supplied by IPT exploiting mainly three alternative options [25]: static wireless charging, quasi-dynamic or dynamic wireless charging. The static IPT consists of the EV charging whenever the vehicle is stationary and nobody stays inside it, e.g. in the case of a parked car. In the quasi-dynamic IPT, the recharge occurs when the electric vehicle is stationary but someone is inside it, e.g. in the case of a cab at the traffic light intersections or a bus at the stop. The dynamic IPT consists in supplying the vehicle during its motion, e.g. in the case of a car running on a highway or of a moving train.

An overview on research and applications about IPT-based wireless charging for some electric means of transportation will be given in the following.

### I.2.1. IPT for E-bike

The Electric Bicycles (E-bikes) are light and compact vehicles, representing a potentially consistent category of transportation means in the current and future scenarios of a smart and green urban mobility.

Due to the generally frequent necessity of using E-bikes during a day and therefore recharging them, the wireless solution may be considered the most appropriate way of E-bike charging**.**

E-bike wireless charging is based on IPT. Academic researchers and commercial operators have proposed different solutions, as far as the position of the coupled coils is concerned. For all the proposed solutions, the E-bike is supposed to be parked in order to have the charging operation.

On the academic side, in [26] and [27] an investigation about different coupling solutions is carried out, all of them consisting of a magnetic coupler made of a transmitter buried underground and a receiver installed inside the bicycle kickstand. Different cases of kickstand are investigated as well. The distance between transmitter and receiver of the magnetic coupler is 2 cm.

In [28], the bicycle coil is placed on the side of the front basket and the grid-connected coil is installed next to a wall, both in a vertical position, as shown in Fig. I.2. The wireless charging operation occurs at a 5 cm distance between the coils.

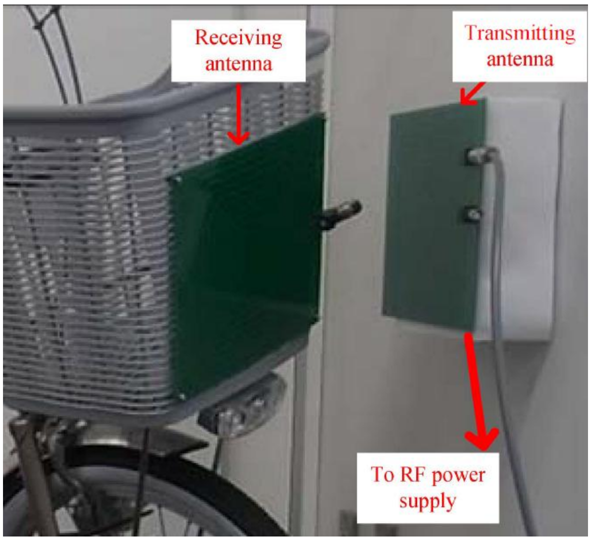

Fig. I.2. E-bike wireless charging proposed in [28]

On the commercial side, *RRC wireless solutions* installs the receiver part under the saddle of the bicycle, as highlighted in Fig. I.3, so that a mechanically movable coil is needed in the transmitter side in order to perfectly align both the sides [29].

Fig. I.3. E-bike wireless charging proposed by *RRC* [29]

*SEW Eurodrive* proposes to put the receiver coil inside the bicycle kickstand [30], as suggested by Fig. I.4.

Fig. I.4. E-bike wireless charging proposed by *SEW Eurodrive* [30]

### I.2.2. IPT for electric car

Implemented through Inductive Power Transfer, the wireless charging for car drivers is convenient as far as safety and comfort are concerned: the user should not be worried about handling power cords, thus avoiding the electrocution risk, and could park the car in proper spaces, so that the charging operation can automatically start. The coils are generally placed in the following way: the one connected to the grid is placed on the ground and the other one, connected to the battery, is placed in the bottom of the vehicle chassis, as suggested by Fig. I.5 [31]. The minimum power level for electric car charging is generally 3 kW.

Different examples of commercial wireless charging stations for electric cars can be provided, since the EV companies are increasingly interested to this innovative charging technology. Among the car manufacturers, *Toyota*, *Nissan*, *General Motors* and *Ford* are some of the companies showing interest in the inductive charging method [32], [33].

Among the companies producing wireless charging systems for EVs, *Evatran* and *HaloIPT* are leaders in providing and improving the inductive charging technology. *Evatran* has created the inducive charging system *Plugless Power*[34]. *HaloIPT*, one of which images of the inductive charger is shown in Fig. I.5, has been acquired by

*Qualcomm* [35]. The opportunity of a fast charging would make the IPT more attractive for EVs [36].

Fig. I.5. IPT-based wireless charging of an electric car [31]

Furthermore, the scientific research is ever more focused on the investigation of different aspects related to the IPT for wireless electric car charging, which are reported in [6], [37–44] and in other scientific work that will be cited in the following of the thesis.

In the realistic scenario of an ever-growing use of EVs, one the most interesting challenges is represented by the possibility of an "on-the-road" charging, meaning that the battery can be recharged while the car is used, as suggested by Fig. I.6.

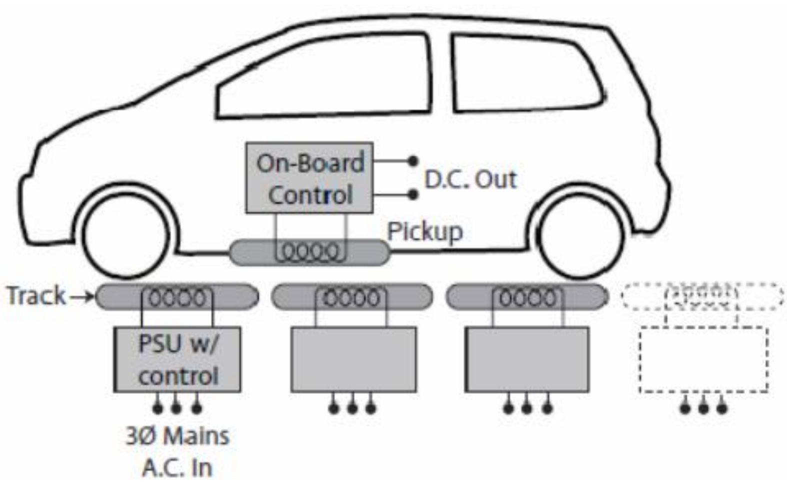

Fig. I.6. Inductively powered roadway [45]

The quasi-dynamic and the dynamic IPT represent an actual solution for the driving range extension of EVs [25]. Different works are reported on this in [46–49]. In [50] and [45] the opportunity of an inductive charging during the motion of the vehicle on highways is investigated.

As suggested by Fig. I.6, in the dynamic charging a track is present inside the road, consisting of multiple transmitting coils, thus allowing the power transfer towards the receiving coil that is inside the car, whenever the receiving coil is aligned, during the motion, to any of the road coils.

The inductive coupling between the electrical grid and the EV can be also exploited for a reverse power flow, that is from the vehicle to the grid. By exploiting reversible power electronics stages, the power is able to flow from the grid to the rechargeable battery and from the battery to the grid, according to the Vehicle-to-grid (V2G) idea. V2G is a wide-spread concept, belonging to the up-to-date idea of the active demand: in a smart electrical network, the consumer is able to become producer of energy. In the case of a surplus of energy stored in some devices of the grid, the power can flow towards other devices requiring energy.

The wireless power transfer can represent a support to V2G, and therefore be a Bi-Directional Inductive Power Transfer (BDIPT). Several works are reported in the scientific literature regarding BDIPT [51–58].

### I.2.3. IPT for electric buses and Railway Applications

Electric buses and railway applications represent ultra-high power levels, from tens to hundreds of kW.

In [59] a detailed review on wireless power transfer for Electric Transit Applications is provided. The *On-Line Electric Vehicle* (OLEV) is one of the most advanced systems for inductive charging of electric vehicles in general and buses in particular [40]. In Fig. I.7. the typical system for the electric bus wireless charging is highlighted.

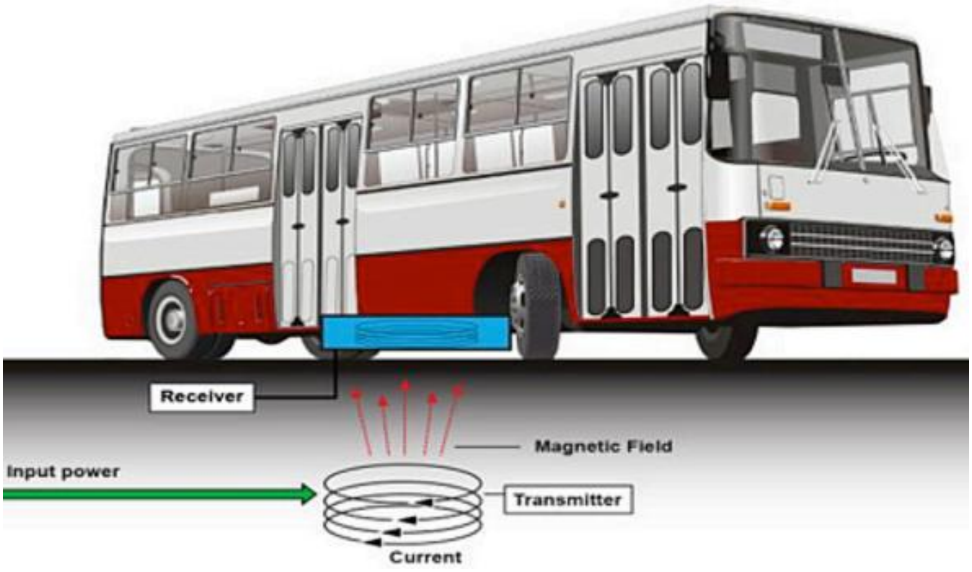

Fig. I.7. Inductive Power Transfer for electric bus charging

In [60] a magnetic coupling structure for IPT applied to railways is proposed. In [61] a study aiming at the efficiency optimization of a Wireless Low Floor Tram (WTRAM) is carried out. *Bombardier* proposes advanced technological solution for the IPT to supply electric buses, trams and trains [62]. A draw of the *Primove* tram by *Bombardier* is shown in Fig. I.8.

Studies have been carried out concerning the use of the Inductive Power Transfer for the supply of the maglev trains. One of the proposed systems is the *Inductive Power Supply for the Transrapid* [63].

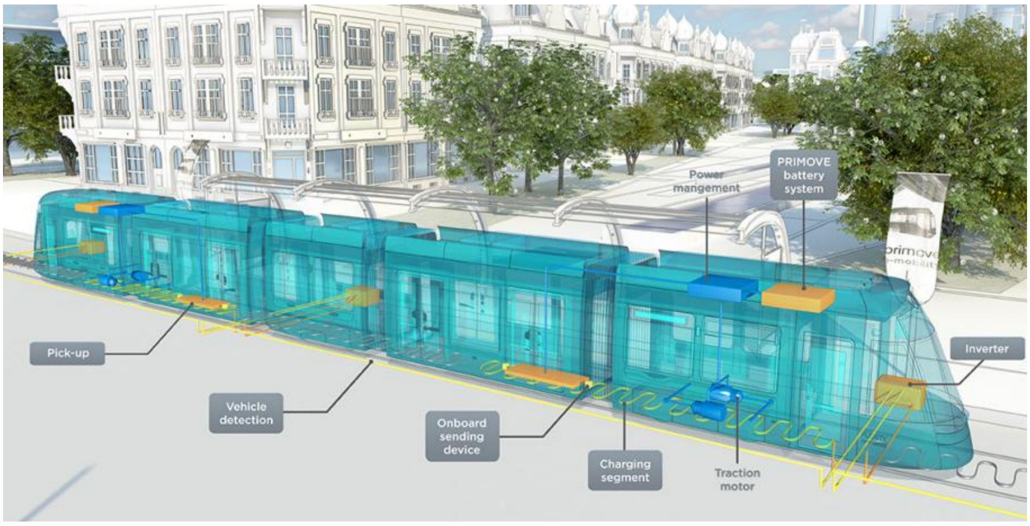

Fig. I.8. *Primove* tram by *Bombardier* [62]

## I.3. The IPT: system description

In Fig. I.9 a typical schematic of an Inductive Power Transfer system is shown. The DC-DC stage is highlighted in the figure. For battery charging applications, the electrical power flows from the DC-link to the battery.

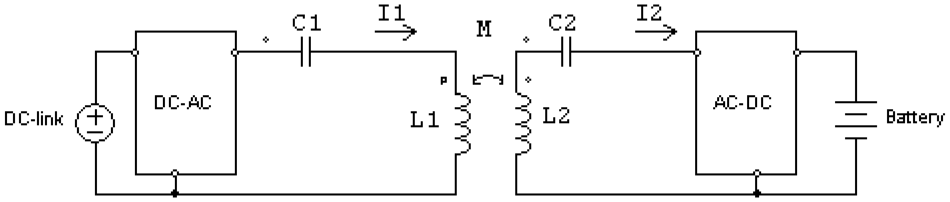

Fig. I.9. A typical schematic of an IPT system

The inductive power transfer occurs between two magnetically coupled coils. Their self-inductances are $L_1$ and $L_2$; the mutual inductance is M. $L_1$ and $L_2$ correspond respectively to the primary and the secondary coil. The primary-side DC voltage source is connected to the electrical grid; the secondary-side DC section is the load representing the battery to be charged. Since the power transfer between the coupled coils is in AC, two intermediate stages are needed: a DC-AC in the primary side and an AC-DC in the secondary side.

Since the coils are loosely coupled, a reactive network is needed in order to maximize the power transfer efficiency and to optimize the power factor, if the system works at the resonance. This reactive network is named compensation circuit and includes two capacitors, one for each side. In the example of the figure, both the compensation capacitors $C_1$ and $C_2$ are connected in series with the primary and the secondary coils.

The main parts of the IPT systems will be described in the following.

### I.3.1. Compensation network

A reactive network is required in order to maximize the power transfer efficiency towards the load and the power factor towards the source. Since the reactive elements needing to be compensated are the coupled inductors, the compensation elements are capacitors. According to Fig. I.9 the capacitor connected to the primary coil is the primary capacitor $C_1$, whereas the capacitor connected to the secondary coil is the secondary capacitor $C_2$.

According to the type of connection between the coils and their compensation capacitors, four different compensation topologies are possible: series-series (SS), series-parallel (SP), parallel-series (PS) and parallel-parallel (PP). For each of these four solutions, the first word (letter) refers to the primary side, whereas the second word (letter) refers to the secondary side, as highlighted in Fig. I.10. Choosing a specific topology rather than another one depends on the specific application [64–69].

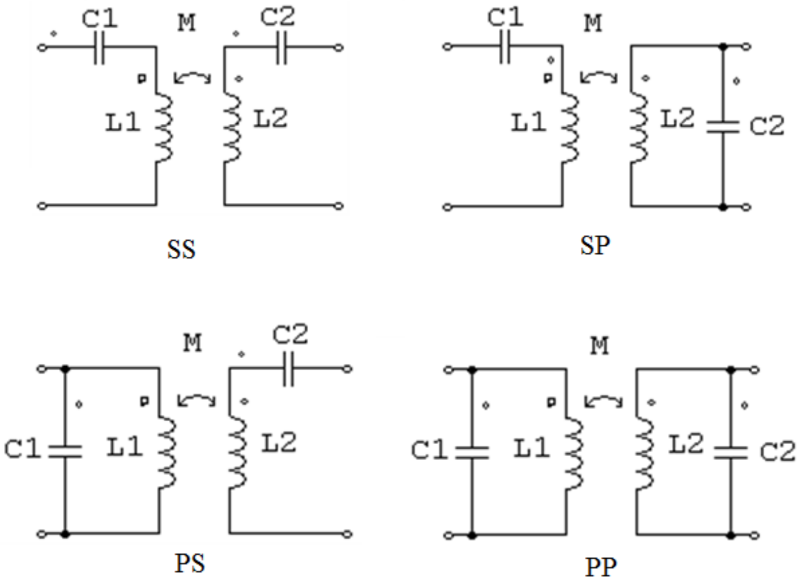

Fig. I.10. The four main compensation topologies

The SS choice allows to select the compensation capacitances depending only on the self-inductances, no matter what the load and the magnetic coupling are. Therefore, in case of misalignments between the coil, the system keeps working under resonance in spite of the mutual inductance variations [70].

For these reasons, the SS topology turns out to be convenient for EV battery charging. Indeed, in IPT charging of vehicles, the perfect alignment between the coils just represents an ideal case and even small misalignments are unavoidable.

### I.3.2. Power converters

Due to the AC nature of the inductive coupling between the coils, the voltages across the primary and the secondary side are alternating. The power source is the electrical grid, whereas the power load is the rechargeable battery. Two power converters are required, one in the primary side and the other one in the secondary side. In the primary side a double stage is generally employed, resulting from the cascade of an AC-DC and a DC-AC (this DC-AC is the one highlighted in Fig. I.9). The goal of this double stage is to increase the power frequency from 50 Hz (or 60 Hz) of the grid to tens of kHz of the IPT. In the secondary side an AC-DC stage is needed in order to supply the DC battery. Since the AC-DC stage in the primary side is quite standard, the scientific research generally focuses on the stage between the primary DC section and the secondary DC section.

Different solutions have been investigated, concerning the primary DC-AC stage and the secondary AC-DC stage. As far as the secondary side is concerned, two possibilities have been mainly exploited to connect the secondary AC side to the DC battery: either a passive rectifier plus a DC-DC converter or an active AC-DC stage.

#### I.3.2.1. DC-AC stage in the primary side

The DC-AC stage in the primary side is supplied by the DC-link and produces the AC waveform useful to produce the alternating current flowing in the primary coil and inducing another current in the secondary coil, as shown in Fig. I.9. In the IPT applied to EV, the frequency of the power signal is some tens of kHz.

Two alternative topologies are possible to implement the DC-AC stage: half-bridge and full-bridge [70].

The half-bridge topology is shown in Fig. I.11. The produced square waveform $V_1$ ranges from $(-V_{dc}/2)$ to $(V_{dc}/2)$, being $V_{dc}$ the DC supply voltage. The duty cycle of $V_1$ corresponds to the duty cycle of the signal driving the two MOSFET gates: when the high-side MOS is on, the low-side is off and vice versa.

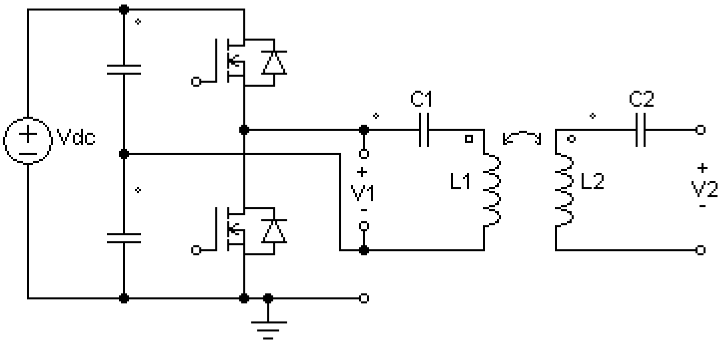

Fig. I.11. A half-bridge DC-AC in the primary side

The full-bridge inverter is shown in Fig, I.12. For the full-bridge topology, the produced AC waveform $V_1$ ranges from $-V_{dc}$ to $V_{dc}$, being $V_{dc}$ the DC supply voltage. Supposing a 50% duty-cycle square waveform $V_1$ for both the half-bridge and the full-bridge, the voltage produced in the full-bridge is twice the corresponding half-bridge voltage. Therefore, to obtain the same power level, the current in the full-bridge can be half of the one in the half-bridge.

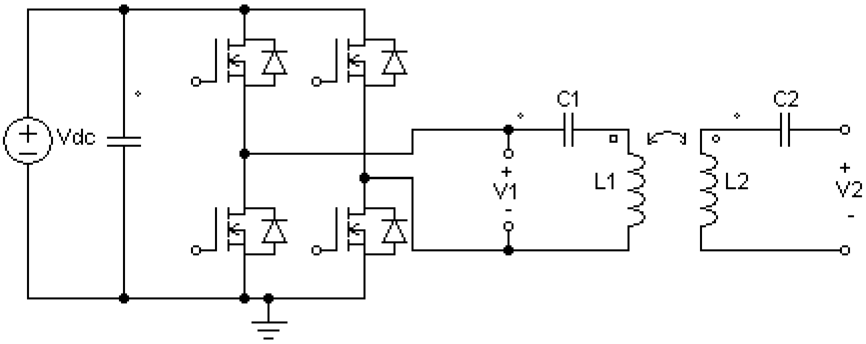

Fig. I.12. A full-bridge DC-AC in the primary side

Due to its four active elements against the only two of the half-bridge, the full-bridge topology is more complex to control: in the half-bridge, only one leg, made of the low-side MOS and the high-side MOS, needs to be driven; in the full-bridge, two legs require to be properly driven. The power flow in the full-bridge can be properly adjusted according to a phase-shift modulation: by controlling the phase difference between the two signals driving the two legs of the full-bridge, the power is regulated.

### I.3.2.2. AC-DC stage in the secondary side

In the secondary side, an AC-DC stage is required to convert the AC voltage arising from the inductive power transfer into a DC voltage useful to supply the battery. According to issues of efficiency and controllability, two alternative solution are usable for the AC-DC stage: a passive rectifier or an active rectifier.

The passive rectifier typically consists of a conventional four-diode bridge which simply rectifies the AC signal arising from the magnetically coupled coils. Nevertheless, the produced DC voltage has to be processed in order to supply the rechargeable battery. Therefore, a DC-DC intermediate stage is required between the passive rectifier and the battery, so that the charging current can be properly controlled. This solution is shown in Fig. I.13.

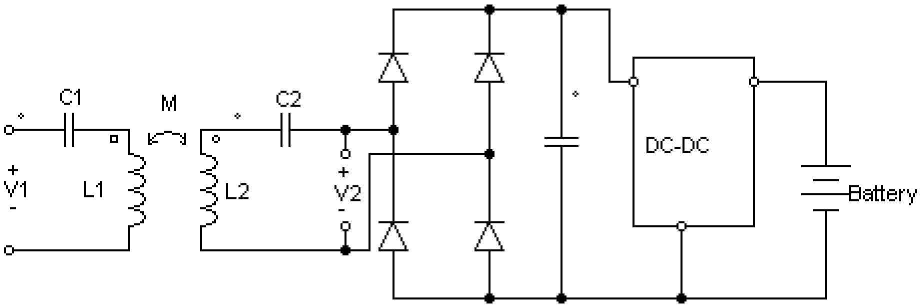

Fig. I.13. A passive rectifier and a DC-DC stage in the secondary side

The drawback of having to use another stage can be avoided by employing an active AC-DC stage. The use of a conventional passive rectifier in the AC-DC stage is not convenient in terms of efficiency and controllability. As far as the efficiency is concerned, the use of active elements is convenient considering the ultra-low resistance of power MOSFETs. As far as the controllability is concerned, an active stage gives the opportunity to directly control the battery charging current, not requiring an additional DC-DC converter to supply the battery.

In Fig. I.14 a 2-diode-2-MOS stage is shown. By controlling the phase difference between the signals applied on the MOSFETs, the amount of power flowing towards the battery is adjustable [71], [72].

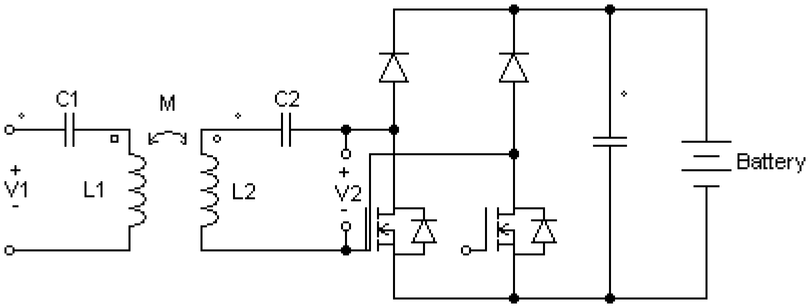

Fig. I.14. A 2-diodes-2-MOS AC-DC in the secondary side

If an entirely active stage is employed, as shown in Fig. I.15, according to the phase difference between the secondary voltage and the primary voltage, the direction of the power flow is adjustable as well. Therefore, an entirely active stage may bring the possibility of a bi-directional power transfer [55], [73].

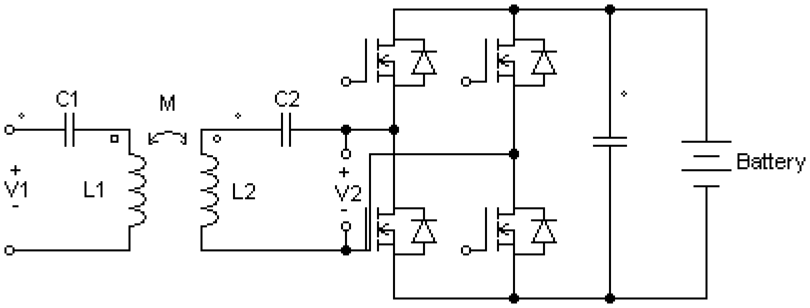

Fig. I.15. A full-bridge AC-DC in the secondary side

### I.3.3. Rechargeable battery

Nowadays the lithium ion batteries represent the most widespread typology of battery, due to their high energy densities and long life-times. The lithium ion batteries well fit with several applications: portable electronics [74], electric vehicles [75], space and aircraft power systems [76], stationary power storage [77].

Among the lithium ion batteries, the Lithium Iron Phosphate ($LiFePO_4$) ones represent an increasing option in the market, particularly for the EVs [78]. $LiFePO_4$ batteries feature high capacity and good stability on chemical and thermal characteristics.

In order to optimize the use of the batteries, a detailed battery model is often required. In [79] and [80], a complete dynamic model of Li-ion batteries, including nonlinear equilibrium potentials, temperature-dependencies, thermal effects and response to transient power demand, is proposed. The model, validated through experimental tests, is useful for the optimization of the battery runtime. In [78], a dynamic model of a $LiFePO_4$ battery is proposed, with particular consideration of the nonlinear capacity effects.

For a proper management of the battery charging system, an accurate knowledge of the current state of charge (SOC) of the battery is needed. In [81] and [82], the authors propose an algorithm for the SOC estimation, according to the nonlinear relationship between the state of charge and the open-circuit voltage of the battery.

A typical charge profile of a Li-ion battery cell is shown in Fig. I.16 [79]. There are mainly two charging modes: constant current mode and constant voltage mode. During the constant current mode, the current is kept fixed at a reference value, while the voltage increases up to a maximum value; then, the constant voltage mode starts, and the voltage is kept fixed at the maximum value, while the current decays to zero.

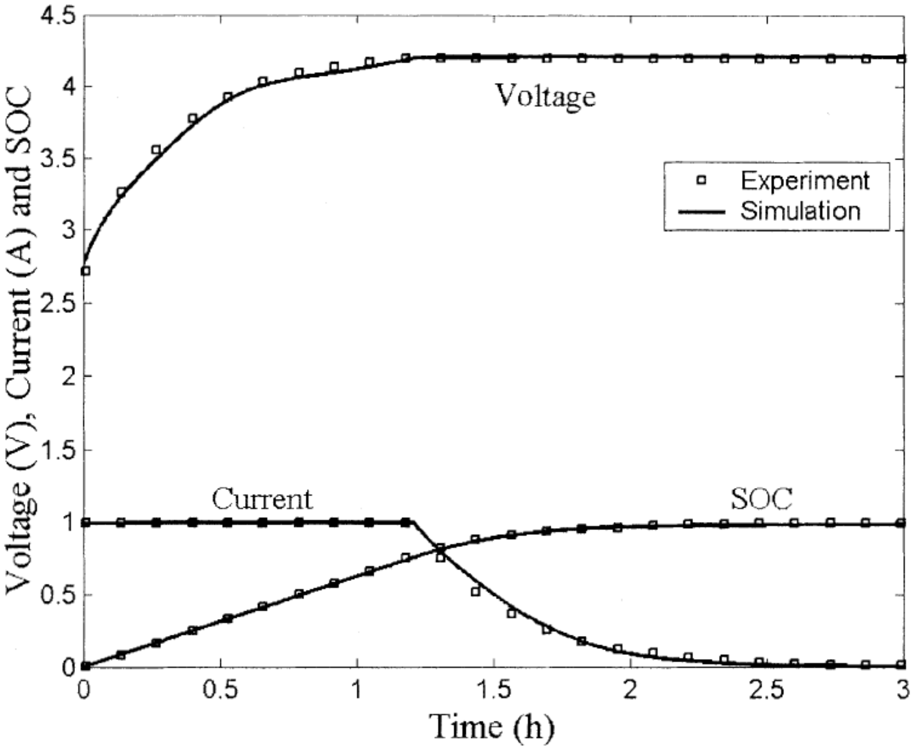

Fig. I.16. Typical charging characteristics of a Li-ion cell [79]

## I.4. IPT and EV applications

The design of an Inductive Power Transfer system applied to an Electric Vehicle is considerably complex since several aspects need to be taken into account. Firstly, an IPT system is made of different electric subsystems requiring to be properly designed and controlled: in the design of the magnetic coupler some care has to be addressed to coupling efficiency, possible misalignments between the coils, weight and bulk; to regulate the amount and the direction of the power flow, the power electronics stages have to be properly controlled. Secondly, the implications arising from the installation and working of an IPT system are diverse: costs, infrastructural works, customer satisfaction, magnetic field exposure and other issues require careful considerations.

In [83] a critical review of the recent progress in wireless power transfer systems and applications is carried out, whereas in [84] an overview of the main IPT technologies for EV battery charging is provided.

In the following, the main aspects related to analysis, design and realization of IPT systems for EVs will be reported, with a reference to the state of the art.

### I.4.1. Analysis and design of IPT systems

For an optimal design, the working principles of different types and topologies of IPT systems should be deeply understood first, independently of applications and power levels. The scientific literature focuses particularly on the maximum efficiency conditions, since the power transfer efficiency is a significant quality index for an IPT system.

In [85] a study on the efficiency maximization, by regulating different parameters such as frequency and mutual inductance, is carried out. An investigation on the relationship between optimal air gap and coil geometry is made as well.

In [86] a method for the efficiency optimization of a series loaded series resonant converter for contactless power transfer systems is suggested, particularly focusing on the regulation of different physical parameters (e.g. transformer ratio, characteristic impedance, operation frequency) and on the investigation of the effects produced by changing the physical separation between both halves of the ferromagnetic core.

The connection between input impedance and maximum transferred power is analyzed in [87], with an experimental validation on two layer square coils.

In [66] and [65] the conditions for the efficiency optimization are evaluated in series-series (SS) and series-parallel (SP) compensation topologies.

The impedance matching problem for IPT systems is investigated in [88], [89].

The bifurcation phenomenon is analyzed in [90–92]. A control oriented to the zero phase angle between input voltage and current should be implemented in order to minimize the VA ratings and therefore power losses and costs. A detailed analysis is carried out with respect to all the possible reactive compensation topologies.

In some cases, such as in Railway Applications, the maximum power transfer is more significant than the maximum efficiency. In [93] the optimal switching frequency for the power transfer is gained: this frequency is different from the resonant frequency, corresponding to the maximum efficiency.

### I.4.2. Magnetic couplers and design methodologies

In the literature, several IPT structures for kWatt automotive applications are tested in order to evaluate magnetic coupling and feasibility. Most of investigated structures include ferrite in order to optimize the power conversion efficiency. Ferrite is yet unfavorable if lightweight power pads are desired. A trade-off between coupling efficiency and weight usually arises. The coupling efficiency is mainly affected by misalignments between the transmitter and receiver coils. For IPT purposes, innovative geometries and core structures are investigated to further reduce the dependence of the power conversion efficiency on misalignments.

In [94] and [95] a circular planar structure with ferrite bars is tested for a 2 kW Inductive Power Transfer. Two identical power pads are employed. Ferrite bars are placed in a radial disposition. The ferrite disk is sliced into bars to reduce the total weight. IPT occurs by means of a current across a planar coil winding placed upon the ferrite bars and following their circular disposition. A single-sided coil winding is used for each of the power pads. The lack of robustness against misalignment in the lateral direction, due to a considerable reduction of magnetic coupling factor for the single-sided configuration, is the main drawback of the specific planar structure. The structure is shown in Fig. I.17.

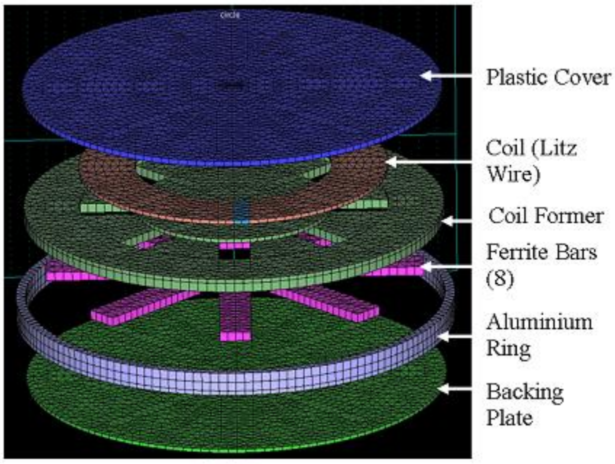

Fig. I.17. Exploded view of an IPT circular pad with ferrite bars and single-sided winding [95]

In [96], the so-called “FluxPipe” magnetic structure consisting of a rectangular planar ferrite core for each power pad is proposed. The coil winding is rolled around the core. Therefore, the winding is “double-sided”. This structure features a more compact size and higher performances than the planar one, due to higher tolerance to lateral misalignments. A photograph of the structure is shown in Fig. I.18.

Fig. I.18. Photograph of the “FluxPipe”, showing the double-sided winding[96]

A maximum 95% coupling efficiency is measured for a 1.5 kW output power and a 7 cm air gap. To lighten the whole structure, tests are also carried out after slicing the core, thus building "split cores". A negligible variation of magnetic coupling is measured, so that the "split-cores" can be employed for an efficient power transfer.

In [39] and [97], the rectangular shape is modified to reduce the weight of the whole structure. A "H-shape" ferrite core is assembled. This structure, shown in Fig. I.19, features almost the same coupling efficiency in comparison with the "FluxPipe", taking advantage from better misalignment-tolerance. Therefore, for electric cars, the H-shape structure represents a better compromise between weight, compactness, tolerance to lateral misalignment and efficiency.

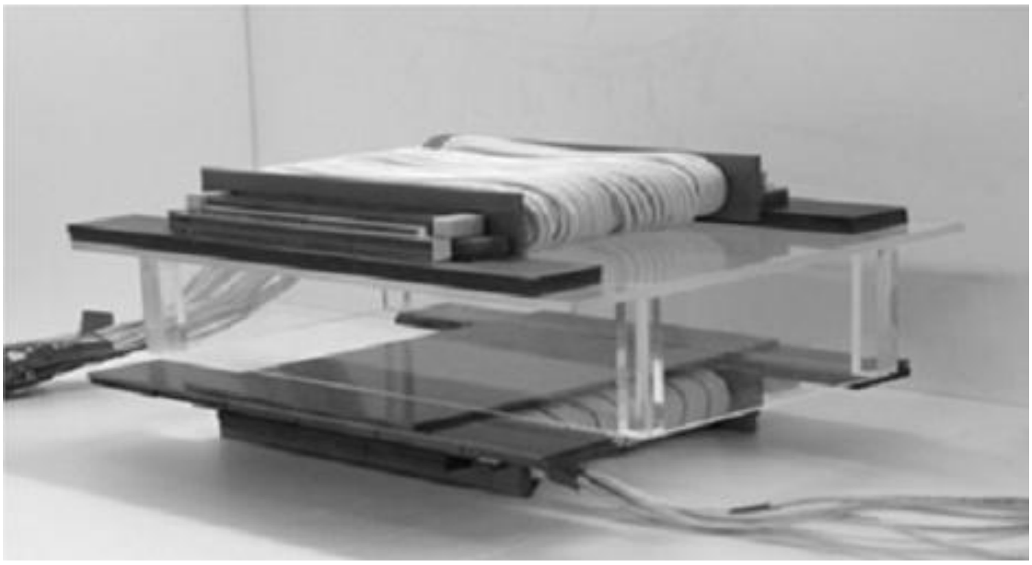

Fig. I.19. Photograph of the "H-shape" structure [39]

Currently, the most attractive shape of magnetic coupler coils for IPT applied to EV wireless charging is the "Double D" (DD), described in [98] and [99] and employed in the works reported in [26] and [100]. In Fig. I.20 a model of the DD solution is shown.

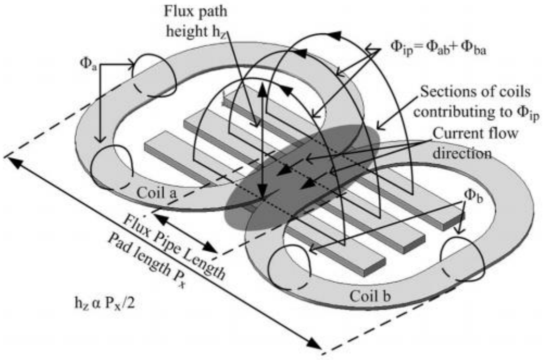

Fig. I.20. Model of the DD coils [98]

In [101] a coreless solution consisting of two circular coils is proposed for wireless EV charging: an investigation on the optimal size of both the coils is carried out, together with a study on the best compensation, which turns out to be the parallel one. An accurate model is built by acquiring the values of mutual inductance corresponding to the different considered dimensions and keeping the air gap length and the structure weight constant. The maximum obtained efficiency is 85% at 20 cm of air gap.

Due to the considerable number of design parameters in the evaluation of a proper magnetic coupling structure, a systematic methodology for the magnetic design can be useful. In [24], a design methodology of magnetic couplers for IPT systems addressed to household appliances and applicable to EV is proposed. Several aspects are considered, such as the tolerance to misalignments and the air gap. By means of ferrite cores, a 90% efficiency at 1 cm of air gap and for 1 kW power level is gained. In [102], a method for the design of a coreless magnetic coupler with rectangular coils is proposed: a 82% efficiency is gained for a 15 cm air gap between the coils, considering a 2 kW prototype. In [100] a standardized magnetic coupler is proposed for wireless EV charging: different sizes of DD (Double D) pads are simulated for different types of use and vehicle. A 10 kW power level can be transferred to charge sedans and SUVs in garage, car-park and roadway locations, considering a 40 cm air gap and a maximum 20 cm horizontal misalignment. In [103] a genetic algorithm is proposed for design and optimization of the track layout of coils for IPT. In [69] a system design methodology is proposed, with particular focus on compensation, stability and control considerations.

### I.4.3. Control strategies

Several control strategies are proposed in literature, in order to properly regulate the IPT system dynamic response and the amount of power flow. In case of Bi-Directional systems (BDIPT), the power flow direction needs to be regulated as well. A general investigation on stability and control of IPT systems for an extended range of power levels (up to 150 kW) is carried out in [104]. In [58] a dynamic control algorithm is provided for a BDIPT system.

In [105] and [106] a comparison between different control strategies for IPT systems is carried out, oriented to high power levels (e.g. EVs) and low power levels (e.g. mobile phones) respectively. In [105] three control methods are mainly compared: phase shift control, frequency control and dual control. The voltage control is not considered due to the requirement of a further power stage, that is a DC-DC converter between the grid side and the primary coil side. The dual control, consisting in a combination of phase shift and frequency control, is proven to be the most convenient in terms of efficiency, stress on the electronic components and controllability.

In [106] four control methods are compared: voltage control, frequency control, duty cycle control and phase shift control. The voltage control is not convenient, requiring a double converter stage. Among the other control strategies, the phase shift control is proven, both from simulations and experimental tests, to be the most convenient as far as costs and stability are concerned. Furthermore, it is compliant with the Qi standard by Wireless Power Consortium, concerning low power devices [20].

An alternative and reliable control method is the power-frequency strategy. In [51] and [55] the relationship between operating frequency and transferred power is exploited to regulate and limit the amount and the direction of the power flow, even if in order to guarantee the maximum efficiency, the system should be kept at the resonant frequency. This control strategy is validated on a 2 kW prototype of BDIPT system. No dedicated communication link is needed. In Fig. I.21 the power-frequency characteristic of a typical BDIPT system is shown, where $f_o$ is the resonant frequency. Based on this, the power-frequency control is developed. The sensitivity of the power-frequency relationship with respect to the variation of the component values is evaluated in [52].

A widely spread control strategy applied to IPT systems, particularly for EV charging and Bi-Directional power transfer, is the phase shift control. The phase shift control consists in the regulation of the power flow amount and direction through some control parameters corresponding to phase angles. In [54] and [107] the phase difference between the fundamental harmonics of primary and secondary voltages is kept at 90° in order to have maximum power factor and maximum efficiency.

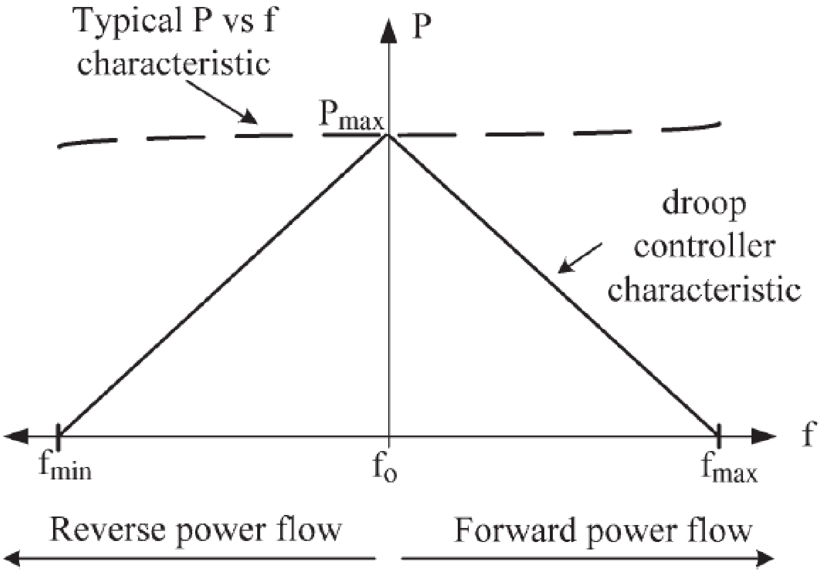

Fig. I.21. Typical Power-Frequency characteristic of a BDIPT system [51]

According to the phase sign, whether the phase angle is +90° or -90°, the direction of the power flow is different, meaning that the power flows from the grid to the battery or from the battery to the grid. Instead, the power flow amount is regulated through the control of the phase angle between the legs of each power converter. In Fig. I.22 a typical block diagram of the phase shift control strategy is shown: α is the actual phase shift.

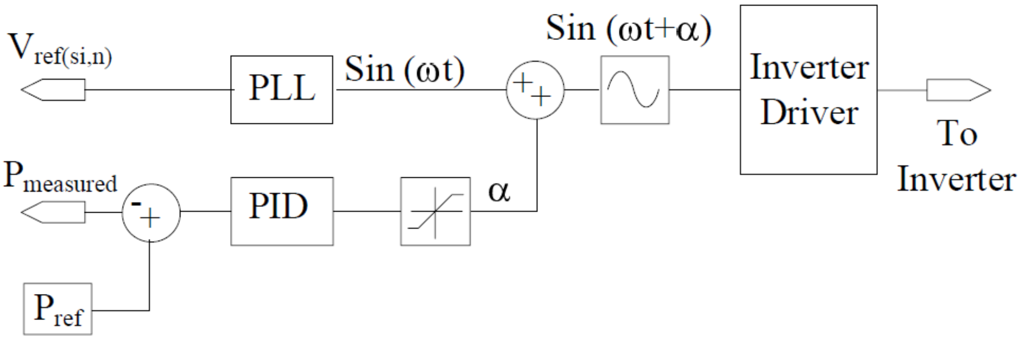

Fig. I.22. Simplified control strategy in a phase shift control [107]

In [108] the phase shift control is applied to an IPT system without compensation network in the secondary side, so that the detuning of this side is unlikely.

In [71] and [72] the phase shift control is exploited to control the power flow towards the battery of a 3 kW EV prototype, charged through IPT. The proposed topology is not usable for BDIPT. A dual-side control allows to improve efficiency and component stress with respect to a single-side control, especially for partial load conditions. Accurate considerations on operating frequency, hard-switching and soft-switching working, technology of the power components, magnetic design and behavior for different air gaps are provided. For the section from the DC source to the battery, the peak efficiency is 95.8% at the minimum air gap of 10 cm.

In [109–111] a control based only on the information arising from the primary side is proposed, in order to avoid the need of a communication link between the power transmitter and the power receiver.

### 1.4.4. Safety considerations

The analysis and the design of wireless battery chargers based on the IPT imply concern for the human safety. Three main sources of hazard should be considered: electrical shock, fire hazards and electromagnetic field exposure.

Electrical shock and fire hazards are inherently due to the high voltages and currents in the primary and secondary coils if high power level systems are considered. Normal care should be taken in order to prevent these cases.

The Electromagnetic Field (EMF) exposure is a major concern for wireless charging, particularly in the case of wireless EV charging. In the IPT systems the operating frequencies generally are equal to tens of kHz, so that the radiation zone is the near field of the electromagnetic field [112]. In the near field region, the field is mainly magnetic. The electric fields are generally more dangerous for the human safety rather than the magnetic fields, so that the radiation produced by the wireless chargers is considered quite safe for the human body [113], [114].

Nevertheless, if the power levels are high, the EMF exposure has to be taken into account for a rigorous consideration of the safety implications. This is the reason why the magnetic field exposure is a major concern for the IPT wireless EV charging, where an accurate investigation on the field distribution should be carried out. Considering the typical case of an electric car wireless charging, for the people inside the vehicle there is not a strong radiation hazard, because of the metal shielding represented by the chassis. The most hazardous radiation zones are between the coils and around the coils. However, these areas are not always directly exposed to humans or animals. In spite of the larger distance from the magnetic coupler, another hazardous zone in need of consideration is the area around the car, because it exposes directly to the general public.

There are mainly two international groups that set standards and guidelines concerning the human exposure to the electromagnetic fields: the International Committee on Electromagnetic Safety (ICES) [115] and the International Commission on Non-Ionizing Radiation Protection (ICNIRP) [116]. These guidelines deal with general public and occupationally exposed population. The standard by ICES also focuses on different parts of the human body in presenting its guidelines.

Few simulation and experimental results have been presented in the scientific literature concerning the radiation produced by IPT-based wireless chargers. In [117] the magnetic coupling structure previously proposed in [92] is investigated also as far as the compliance with the ICNIRP exposure limits is concerned. The particular combination of cylindrical shape and ferrite disposition aims at containing most of the magnetic flux inside the coupling structure, so that the flux density decreases rapidly outside the charger. Nevertheless, experimental results concerning the radiation are not provided in this work. Apart from the direct coupling to the body, sometimes an indirect coupling can occur as well. Examples of potential indirect coupling are the EMF coupling to medical implantable devices or the physical contact of the body with objects which are strongly exposed to the magnetic field [112].

In this Chapter the main applications of wireless battery charging have been addressed, considering the power levels ranging from the µW of Wireless Sensor Networks (WSN) to the hundreds of kW of Railway Applications, passing through the following applications: electric toothbrush, consumer electronic devices, household appliances and Electric Vehicles (EVs). A technical background on the Inductive Power Transfer systems has been given, particularly focusing on the electronic and the magnetic design. A general overview and the state of the art concerning the IPT applied to the EVs have been provided, considering magnetic couplers, design methodologies, control strategies and safety issues.

In the next two Chapters the contribution of this thesis will be reported. The proposed work focuses mainly on the E-bike application. An IPT system for the wireless battery charging of an electric bicycle will be proposed, with particular attention on the magnetic and the electronic design issues.

After that, an analytical study on a typical Bi-Directional IPT system will be provided. This work has contributed to deeply understand the power flow in a BDIPT system as function of different control parameters. The analytical results have been validated through electronic simulations.

A control algorithm for the maximization of the power transfer efficiency will be proposed as well. This algorithm represents an original research contribution, since a power tracking method aiming at the efficiency optimization in IPT systems was not known in the scientific literature.

Alternative solutions of inductive coupling will be investigated as well, according to a deep analysis through a 3D magnetic simulator. An optimal solution in terms of efficiency and tolerance to misalignments will be proposed as far as wireless E-bike battery charging is concerned.

The experimental results in terms of power transfer efficiency and magnetic characterization of the assembled prototype will be explained, focusing particularly on the coupling efficiency and on the physiological compatibility of the system.

# Chapter II

## Design of an IPT system for E-bike battery charging

The Inductive Power Transfer (IPT) can be exploited for Electric Vehicle (EV) battery charging. The IPT consists of a wireless power flow between two magnetically coupled coils. Therefore, through IPT the battery charging can occur wirelessly. The lack of wires brings some benefits in terms of comfort and safety: the vehicle could be automatically charged without the need of a plug-in operation and no electrocution risk would involve the user.

Depending on whether the vehicle is stationary or in motion, and whether the driver is inside the vehicle or not, there are three types of IPT-based battery charging: static, semi-dynamic and dynamic [25]. The static IPT occurs when the vehicle is stationary and nobody is inside it, i.e. during the parking time; the semi-dynamic IPT occurs when the vehicle is stationary and the driver is inside it, i.e. during the stop at traffic red lights for cars or during the bus stop for electric buses; the dynamic IPT occurs when the car is in motion, i.e. along motorways.

Yet the dynamic wireless battery charging features some drawbacks. The motion of the vehicle implies a widespread infrastructure of power transmission buried inside the road in order to have adequate charging times and therefore for an efficient dynamic charging high costs are required.

IPT is cheaper in static and semi-dynamic options, since the same charging time is covered by the use of a minor number of coils in comparison with the dynamic case, due to the stationary state of the vehicle. Static IPT is feasible for private EVs which could stay stationary for some hours, whereas semi-dynamic IPT is particularly appropriate for public electric means of transportations, such as cabs or buses, needing to continuously move across the day and therefore requiring frequent charging operations if a proper autonomy is wanted without increasing the battery size.

Considering that the wireless battery charging is inherently less efficient than the conventional wire-based battery charging, the benefits brought by the wireless method in terms of comfort and safety need to be notable in order to make the static IPT really attractive for EV battery charging.

The frequent movements of a vehicle may require to charge its battery many times across the whole day. This particularly fits with the case of electric bicycles, being very smart and comfortable to be driven in the congested traffic, typical of the urban scenario. The bike is potentially an ideal means of transportation for frequent transfers throughout the day. Furthermore, the E-bike represents a smart, green and light solution of urban mobility. More and more people are supposed to be driving electric bicycles in the next future. IPT would therefore represent a brilliant solution of battery charging for parked E-bikes, due to different reasons. First of all, every time the cyclist parks the E-bike, it would be automatically recharged without the bothersome and potentially dangerous plug-in operation. Later, in case of multiparking areas for E-bikes, each bicycle could be recharged and no wire would be visible.

In the next paragraphs an IPT system for E-bike wireless battery charging will be proposed. After a general description of a typical IPT system, the single subsystems will be described and the design criteria which have been followed for the proposed system will be explained. The here proposed IPT system aims at charging a 36 V 10 Ah $LiFePO_4$ battery. The maximum flowing power can range from 100 W to 250 W.

The papers [118–121] have resulted from this work.

## II.1. Design of the IPT system

In Fig. II.1 the DC-DC stage model of the proposed IPT system for wireless E-bike battery charging is shown, recalling Fig. I.9. As far as the actual inductive power transfer is concerned, the self-inductances related to the coupled coils are $L_1$ and $L_2$, whereas the mutual inductance is M. $L_1$ and $L_2$ correspond respectively to the primary and the secondary coil. The primary-side DC voltage source is connected to the electrical grid; the secondary-side DC section is the load representing the battery to be charged.

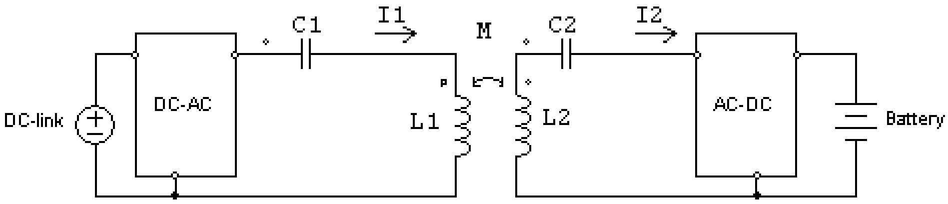

Fig. II.1. The functional model of the proposed IPT system

A SS capacitive compensation is proposed, as highlighted by the figure, being both $C_1$ and $C_2$ connected in series with the coupled coils. This choice allows to select the compensation capacitances depending only on the self-inductances: this choice is therefore independent of the load and the magnetic coupling [70].

In addition to this, as explained in the following, the SS choice allows to easily manage the main battery charging mode, which is the constant current mode.

For the electric car battery charging, the IPT usually consists of a transmitter coil placed on the road and a receiving coil placed on the bottom part of the chassis [25], [39], [84].

As far as the E-bike IPT battery charging is concerned, the scientific literature provides few works [26–28]. The commercial actors provide few examples as well [29], [30]. In [27], [26] and [30], the receiving coil is mounted on the kickstand, whereas the transmitting coil is buried inside the pavement. In [28], the bicycle coil is placed on the side of the front basket and the grid-connected coil is installed next to a wall, both in a vertical position, as shown in Fig. I.2. The wireless charging operation occurs at a 5 cm distance between the coils. In [29], the receiver part is under the saddle of the bicycle, as highlighted in Fig. I.3.

In the proposed E-bike wireless battery charging system, the supposed position for the receiver coil is on the bicycle front wheel, parallel to it. While the bicycle stands in public parking areas, the front wheel is supposed to be fixed to a support. The power transmitter could house inside this support.

A compact solution of magnetic coupling is therefore well-suited for this application. A flat structure seems to be appropriate and a circular shape properly fits with the wheel. Ferromagnetic materials are generally exploited for EV wireless charging in order to reduce the leakage magnetic flux, thus optimizing the power transfer efficiency even for large air gaps between the coils [94], [96–98], [100].

For the proposed E-bike IPT system no ferromagnetic material is employed, in order to obtain a light-weight, compact and cheap structure.

In IPT systems for EV battery charging, the current trend is to build a large transmitter coil and a smaller receiver coil. The reduced size of the receiver coil is generally due to the space restrictions in a movable system like a vehicle. The larger size of the transmitter coil allows to produce high amounts of power, thus creating a more uniform magnetic field in the receiver region [122], [123]. Nevertheless, in the proposed system, primary and secondary coil windings have been chosen identical in order to minimize the total leakage flux. This represents the conventional solution for loosely coupled coils [24], [41]. In addition to this, due to its geometrical symmetry, this choice fits the possibility of a bi-directional power transfer. In a Bi-Directional IPT (BDIPT) system, the power can flow not only from the grid to the battery, but also in the opposite direction [57], [58].

In the BDIPT, the role of power transmitter or power receiver can be alternatively played by both the coils: in the grid-to-battery power flow the primary coil is the power transmitter and the secondary coil is the power receiver; in the battery-to-grid power flow the secondary coil is the power transmitter and the primary coil is the power receiver. The interchangeability of power transmitter and power receiver can be guaranteed by reversible DC-AC and AC-DC stages, being able to respectively convert into an AC-DC and a DC-AC in the transition from a grid-to-battery to a battery-to-grid power flow.

The diameter of each coil has been chosen according to space constraints in the E-bike wheel. The number of turns of each coil is oriented to a trade-off between different aspects: the coupling coefficient, the power losses due to the length of the wire, the skin effect, the bifurcation phenomena. This trade-off is well explained in [121].

In order to evaluate the electrical features of the coupled coils according to the number of turns, a magnetic field simulation has been implemented through a FEM 2D software, that is a magnetic simulator based on Finite Element Method [124]. The

3D problem has been converted into a 2D problem due to the cylindrical symmetry of the geometry. The symmetry axis passes through the centers of the circular coils.

Each coil features a 15 cm outer diameter, and 9 turns of copper wire, with a 3 mm section diameter. Considering a 3.5 mm space between the wire section centers of two consecutive turns, a 8.8 cm inner diameter results. A 3 cm air gap between the parallel windings is chosen as maximum value in order to test the coupling efficiency of the designed IPT system. In Fig. II.2 a 3D model of the proposed magnetic coupling structure is shown.

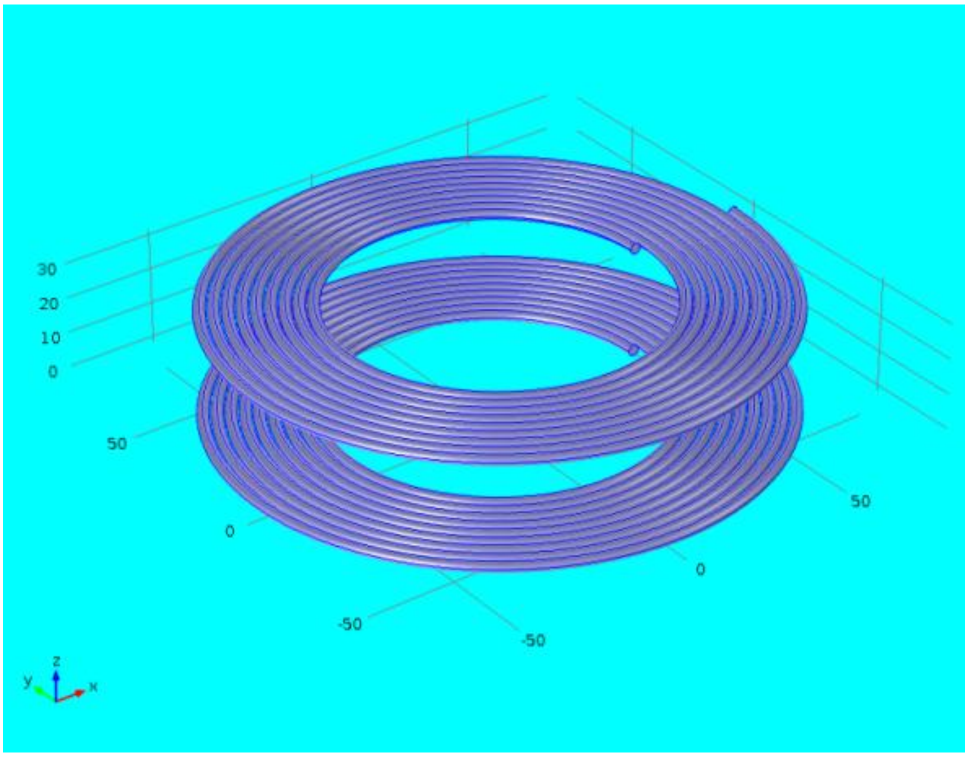

Fig. II.2. 3D model of the proposed flat circular coils

The features of the proposed coupling structure, concerning material and geometries, are summed up in Tab. II.1: $\rho_{Cu}$ and $\mu_{r,Cu}$ are the electric resistivity and the relative magnetic permeability of copper; d is the diameter of the wire section; l is the total length of the wire of each coil; $d_{out}$ is the outer diameter of the flat circular coil; N is the number of turns.

The air gap is the separation between the coils.

TABLE II.1.

CHARACTERISTICS OF THE PROPOSED COUPLING STRUCTURE

| **Material** | **Value** |
|---|---|
| $\rho_{Cu}$ | $1.68 \cdot 10^{-8}\ \Omega \cdot m$ |
| $\mu_{r,Cu}$ | ~1 |
| **Wire geometry** | **Value** |
| d | 3 mm |
| l | 3.48 m |
| **Coil geometry** | **Value** |
| $d_{out}$ | 15 cm |
| N | 9 |
| maximum air gap | 3 cm |

Fig. II.3 shows the simulation file, in the vertical section view, which completely describes the problem due to the axisymmetric shape of the object. The colors refer to different values of the resulting magnetic field in the region around the coils. Through a post-processing operation, the magnetic features of the coupled coils have been calculated by the simulator. Magnetostatic simulations have been performed, supposing that the magnetic parameters are frequency-independent if a (0÷150) kHz frequency range is considered, since 150 kHz is the maximum value of the IPT system frequency that has been considered.

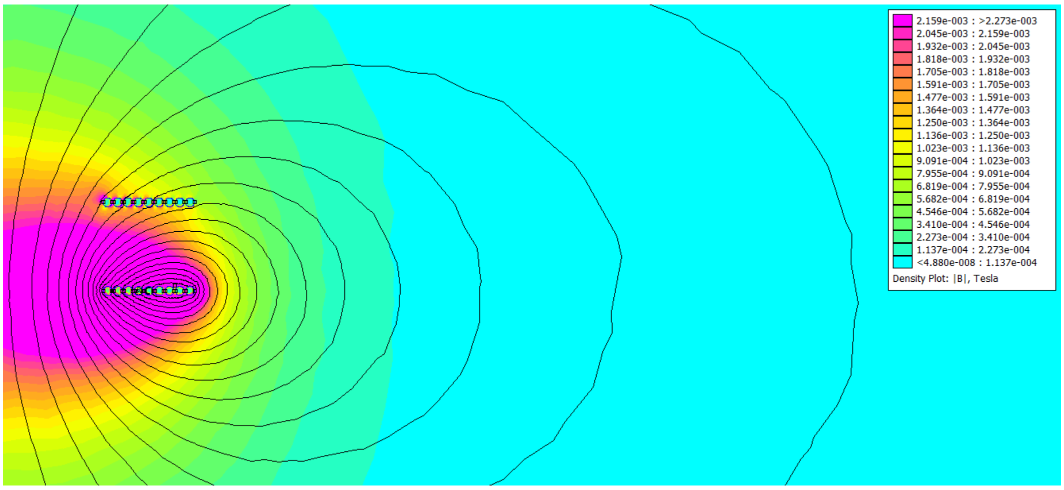

Fig. II.3. Magnetic flux density simulation results arising from the 2D model of the proposed coupling structure

The magnetic field has been produced by injecting a 26 A current into the upper coil, referring to the figure.

In order to obtain the primary self-inductance $L_1$, the flux of this magnetic field through the surface of the same coil has been considered, and the secondary self-inductance $L_2$ is supposed to be the same since the coils are identical. The common value of the self-inductances is represented by L. To obtain the mutual inductance M, the flux of the magnetic field through the surface of the lower coil, referring to the figure, has been considered. The electric model features of the magnetic coupling structure, as obtained from *FEMM* analysis by setting a 3 cm air gap, are listed in Tab. II.2. k is the coupling coefficient of the magnetic structure. The relationship between mutual and self-inductances is given by:

$$M = k\sqrt{L_1 L_2} = kL \tag{II.1}$$

**TABLE II.2.**

ELECTRIC CHARACTERIZATION OF THE PROPOSED COUPLING STRUCTURE

| **Element** | **Value** |
|---|---|
| $L_1 = L_2 = L$ | 13 µH |
| M | 4.9 µH |
| k | 0.377 |
| $R_{dc}$ | 8.2 mΩ |

$R_{dc}$ is the DC resistance of each coil, arising from the copper resistivity $\rho_{Cu}$, the length l and the section area A (corresponding to the area of a circle whose diameter is 3 mm), according to the second Ohm law, that is the following:

$$R_{ohm} = \frac{\rho_{Cu} \cdot l}{A} \tag{II.2}$$

In Fig. II.4 the simulation model of the proposed IPT system is shown.

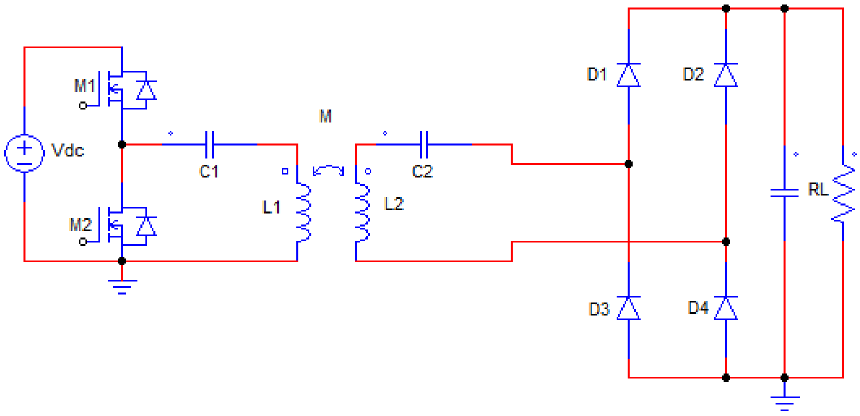

Fig. II.4. Simulation model of the IPT system, created through *PowerSIM* software [125]

The DC-AC in the transmitter side is implemented through a half-bridge topology (MOSFETs M1-M2); the AC-DC in the receiver side is a conventional four diode rectifier. The electric model parameters of the coupled coils arise from the electric characterization summed up in Tab. II.2. A 2 A current generator works as load of the system, emulating the battery charging current. The compensation series capacitors have a 220 nF value, arising from the choice of a working frequency close to 100 kHz. Being this system designed for an experimental test, commercial values of capacitance have been chosen. The actual frequency is therefore 94.1 kHz, arising from the following expressions:

$$f_1 = \frac{1}{2\pi\sqrt{L_1 C_1}} \qquad f_2 = \frac{1}{2\pi\sqrt{L_2 C_2}} \tag{II.3}$$

$f_1$ and $f_2$ are respectively primary and secondary resonant frequencies, which shall be equal to each other if the double goal of maximum power factor and maximum power transfer has to be achieved. Therefore, since identical planar coils are designed, identical values of $C_1$ and $C_2$ are obtained.

The design specifications are reported in Tab. II.3.

**TABLE II.3.**

DESIGN SPECIFICATIONS

| Specification | Value |
|---|---|
| Rated Load Power | 96W |
| Nominal DC bus voltage | 48V |
| Rated current | 2A |
| Operating frequency | 94.1kHz |

## II.2. Bi-Directional Inductive Power Transfer (BDIPT)

IPT well fits with the idea of a “Bi-Directional” power transfer, meaning that the power is able to flow from the grid to the load or, alternatively, from the load to other users of the grid. A Bi-Directional Inductive Power Transfer (BDIPT) system is therefore exploitable to accomplish the Vehicle-To-Grid (V2G) concept, consisting in the possibility to use the EV battery as storage element for other users of the grid or other vehicles as well, in the scenario of a multi-parking area. The V2G idea belongs to the philosophy of the active demand, where the user plays the double role of consumer and producer of electrical energy.

In Fig. II.5 the model of a BDIPT system is shown.

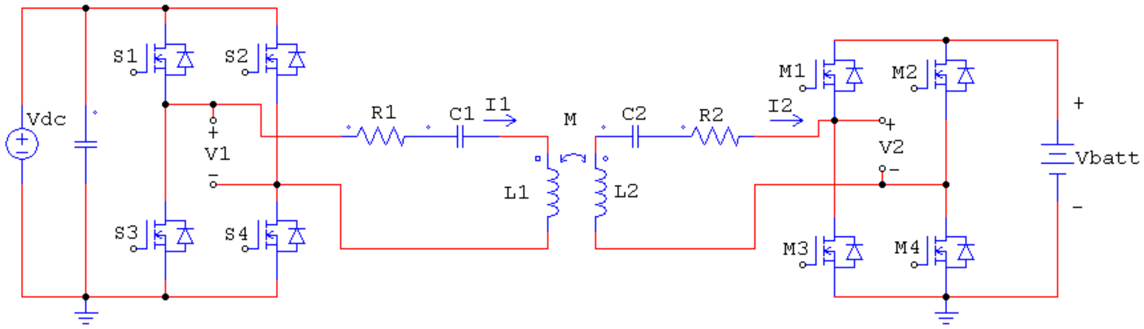

Fig. II.5. Model of a BDIPT system

The compensation capacitive topology is the one proposed for the assembled prototype, that is series-series (SS). $R_1$ and $R_2$ represent the power losses in the primary and secondary side respectively. The DC-AC stage from $V_{dc}$ to the primary side and the AC-DC stage from the secondary side to $V_{batt}$ are two reversible rectifiers: the primary full-bridge converter (S1-S2-S3-S4) producing the AC waveform $V_1$ and the secondary full-bridge converter (M1-M2-M3-M4) producing the AC waveform $V_2$. Depending on the phase delay between $V_1$ and $V_2$, the power flow direction can be determined. If a power transfer aiming at the battery charging is desired, a phase lead of $V_2$ with respect to $V_1$ shall occur. If maximum power factor is desired, the phase lead is set at 90°. In the following, a detailed mathematical analysis of this BDIPT circuit, concerning the power flow and its dependence on several parameters, will be carried out.

### II.2.1. Mathematical analysis of the system power flow

In order to control the amount and the direction of the power flowing in the BDIPT system, a circuital analysis has been carried out. A computational support has been provided by the software *MATLAB Simulink* [126]. Arising from the schematic in Fig. II.5, a simplified model can be built, as shown in Fig. II.6.

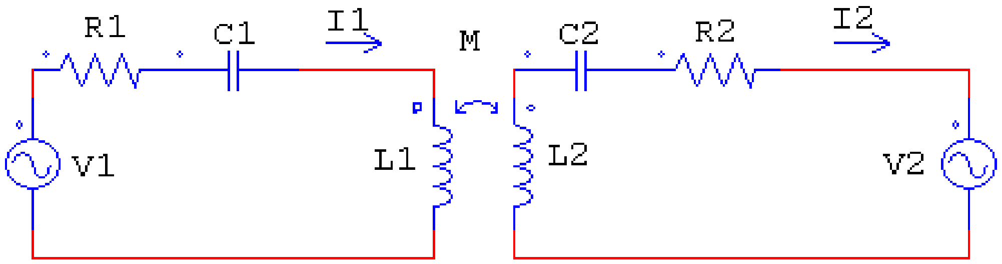

Fig. II.6. The IPT system with the AC waveforms $V_1$ and $V_2$ in evidence

The AC voltage sources represent the primary and secondary waveforms produced by the DC-AC stage and the AC-DC stage respectively, according to Fig. II.1.

From the circuit shown in Fig. II.6, the following system of phasorial equations arises:

$$\begin{aligned}\vec{V}_1 &= \left[ j\omega(L_1 - M) + j\omega M + \frac{1}{j\omega C_1} + R_1 \right]\vec{I}_1 - j\omega M\vec{I}_2 \\ j\omega M\vec{I}_1 &= \left[ j\omega(L_2 - M) + j\omega M + \frac{1}{j\omega C_2} + R_2 \right]\vec{I}_2 + \vec{V}_2\end{aligned} \tag{II.4}$$

In the simple case of two square waveforms at the primary and the secondary full-bridges and considering $V_1$ and $V_2$ as the amplitudes of the phase-modulated voltages in the primary and in the secondary side respectively, the amplitudes of their fundamental harmonics are $\frac{4}{\pi}V_1$ and $\frac{4}{\pi}V_2$ . Therefore, the RMS values are $\frac{2\sqrt{2}}{\pi}V_1$ and $\frac{2\sqrt{2}}{\pi}V_2$ respectively. Subsequently the phasors linked to $V_1$ and $V_2$, considering that $\varphi_1$ and $\varphi_2$ are their phases, with respect to a zero phase reference phasor, are given by:

$$\begin{aligned}\vec{V}_1 &= \frac{2\sqrt{2}}{\pi}V_1\left(\cos\varphi_1 + j\cdot\sin\varphi_1\right) \\ \vec{V}_2 &= \frac{2\sqrt{2}}{\pi}V_2\left(\cos\varphi_2 + j\cdot\sin\varphi_2\right)\end{aligned} \tag{II.5}$$

The phase delay $\varphi_D$ is defined as the phase difference between $V_2$ and $V_1$, whereas the phase shift $\varphi_S$ is defined as the phase difference between the signals applied to the two legs of the full-bridge converter. Therefore, this expression arises for the phase delay:

$$\varphi_D = \varphi_2 - \varphi_1 \tag{II.6}$$

The real power on the primary and secondary sides are:

$$\begin{aligned}P_1 &= \mathrm{Re}(\vec{V}_1\vec{I}_1^{\,*}) \\ P_2 &= \mathrm{Re}(\vec{V}_2\vec{I}_2^{\,*})\end{aligned} \tag{II.7}$$

From (II.4), the phasor of the primary current arises:

$$\vec{I}_1 = \frac{\vec{V}_1 - \dfrac{j\omega M\vec{V}_2}{R_2}}{R_1 + \dfrac{(\omega M)^2}{R_2}} \tag{II.8}$$

The conjugate phasor of the primary current is therefore:

$$\vec{I}_1^* = \frac{2\sqrt{2}}{\pi}\left[\frac{V_1(\cos\varphi_1 - j\cdot\sin\varphi_1) + \dfrac{\omega M V_2}{R_2}(\sin\varphi_2 + j\cdot\cos\varphi_2)}{R_1 + \dfrac{(\omega M)^2}{R_2}}\right] \tag{II.9}$$

According to (II.5), (II.7) and (II.9), the real power on the primary side is:

$$P_1 = \frac{8}{\pi^2}\left[\frac{V_1^2 + \dfrac{V_1 V_2 \omega M}{R_2}\sin\varphi_D}{R_1 + \dfrac{(\omega M)^2}{R_2}}\right] \tag{II.10}$$

From (II.4), the phasor of the secondary current arises:

$$\vec{I}_2 = \frac{\dfrac{j\omega M\vec{V}_1}{R_1} - \vec{V}_2}{R_2 + \dfrac{(\omega M)^2}{R_1}} \tag{II.11}$$

The conjugate phasor of the secondary current is therefore:

$$\vec{I}_2^{*} = \frac{2\sqrt{2}}{\pi}\left[\frac{\frac{\omega M V_1}{R_1}\left(-\sin\varphi_1 + j\cdot\cos\varphi_1\right) - V_2\left(\cos\varphi_2 + j\cdot\sin\varphi_2\right)}{R_2 + \frac{(\omega M)^2}{R_1}}\right] \tag{II.12}$$

According to (II.5), (II.7) and (II.12), the real power on the secondary side is:

$$P_2 = \frac{8}{\pi^2}\left[\frac{\frac{V_1 V_2 \omega M}{R_1}\sin\varphi_D - V_2^2}{R_2 + \frac{(\omega M)^2}{R_1}}\right] \tag{II.13}$$

The actual RMS of the primary and secondary waveforms are linked to the DC voltages V$_1$ and V$_2$ according to their values of phase shift, $\varphi_{s1}$ and $\varphi_{s2}$, referring respectively to the primary and to the secondary full-bridge:

$$\begin{aligned} V_1 &= V_{dc}\sin\left(\frac{\varphi_{s1}}{2}\right) \\ V_2 &= V_{batt}\sin\left(\frac{\varphi_{s2}}{2}\right) \end{aligned} \tag{II.14}$$

Replacing (II.14) in (II.10) and (II.13), the real powers are obtained:

$$\begin{aligned} P_1 &= \frac{8}{\pi^2}\frac{V_{dc}\sin\left(\frac{\varphi_{S1}}{2}\right)}{R_1 + \frac{(\omega M)^2}{R_2}}\left[V_{dc}\sin\left(\frac{\varphi_{S1}}{2}\right) + \frac{V_{batt}\,\omega M\sin\left(\frac{\varphi_{S2}}{2}\right)\sin(\varphi_D)}{R_2}\right] \\ P_2 &= \frac{8}{\pi^2}\frac{V_{batt}\sin\left(\frac{\varphi_{S2}}{2}\right)}{R_2 + \frac{(\omega M)^2}{R_1}}\left[\frac{V_{dc}\,\omega M}{R_1}\sin\left(\frac{\varphi_{S1}}{2}\right)\sin(\varphi_D) - V_{batt}\sin\left(\frac{\varphi_{S2}}{2}\right)\right] \end{aligned} \tag{II.15}$$

This circuital analysis has been validated through power electronics simulations [125].

[127] and [128] have resulted from this work, including also an efficiency optimization algorithm which will be explained in the following.

### II.2.2. Investigation on alternative coupling solutions

In order to improve the efficiency and the tolerance to potential misalignments between the coils, different magnetic coupling structures have been compared to the assembled one. The characterization of the inductive coupling solutions, aiming at evaluating their influence on the whole IPT system, has been carried out trough 3D magnetic simulations. [129] has resulted from this work of investigation.

The investigation has been made taking into account the system of Fig. II.5, so that a Bi-Directional power transfer is possible. The equations (II.15) have been considered for the estimation of the system efficiency. A 90° phase delay $\varphi_D$ has been chosen. The considered values of supply voltage $V_{dc}$ in the primary side and battery voltage $V_{batt}$ in the secondary side are given in Tab. II.4.

**TABLE II.4.**

DC VOLTAGES IN THE INVESTIGATED SYSTEM

| **DC supply voltage** | **Value** |
|---|---|
| $V_{dc}$ | 24 V |
| **Battery voltage** | **Value** |
| $V_{batt}$ | 36 V |

Different structures of inductive coupling are investigated in terms of system efficiency and tolerance to misalignments. The goal is to find the best solution in compliance with an E-bike wireless battery charging system. The investigated solutions consist of two flat winding coils; each of them features a copper wire, with a 3 mm diameter section. The pitch between two consecutive turns is 3.5 mm.

The proposed structures imply two identical coils, thus minimizing the total leakage flux and well fitting the case of a bi-directional power transfer. No ferromagnetic material is used in order to lighten the weight of the structure, taking into account the E-bike application. As for the previously proposed structure, one coil is supposed to be placed upon a wheel of the bicycle; the other one is supposed to be placed on the support holding up this wheel during the parking time.

The equivalent electric model concerning each investigated option is gained after several magnetic field simulations. The software *COMSOL Multiphysics* has been used as modeling and simulation tool working in a 3D geometry [130]. Different distances and misalignments between the primary and the secondary coil have been taken into account to obtain thorough models in terms of self-inductances and mutual inductance.

The first option to be considered consists of two circular coils. This solution is applied on the actually assembled prototype of E-bike wireless charger. The 3D model of this option has been already shown in Fig. II.2. Each coil consists of a flat helix winding, featuring 9 turns and a 15 cm outer diameter.

As for the next considered options, the coils lie on the x-y plane, whereas the distance between them belongs to the z axis.

The other investigated solutions are based on the DD shape [98]: each coil is made of two square parts, the so-called “D”, which are connected in series. The result is that there is a continuous magnetic flux loop inside the structure including the two DD coils. This should create a structure inherently tolerant to misalignments between the two coils. The longest dimension is kept under 30 cm in order to well fit the size of a bicycle wheel. Fig. II.7 shows the 3D model of the DD option. The whole winding coil consists of two “D-shaped” parts. Each “D” is a flat square winding made of 9 turns. In compliance with the size of a bicycle wheel, for the proposed option three different sizes are tested. Keeping the shape and the proportions of the whole structure for each coil, the length of the shortest side belonging to the smallest square (labeled “s” in the figure) is modified according to the following three values: 4 cm, 5 cm, 6 cm. The corresponding values of the longest size, that is the side along the y axis, are the following ones: 21 cm, 23 cm, 25 cm. For each proposed option, the magnetic field simulations are carried out considering different distances and misalignments between the two coils. The air gap between the coils ranges from 1 cm to 3 cm on the z axis, whereas the misalignment on the x-y plane ranges from 0 to 2 cm for each of the two axes.

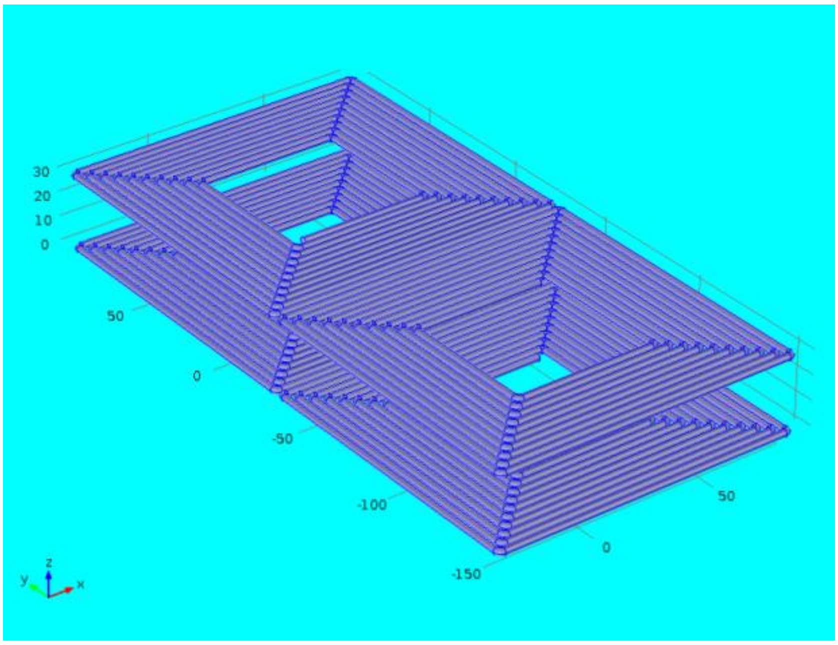

(a)

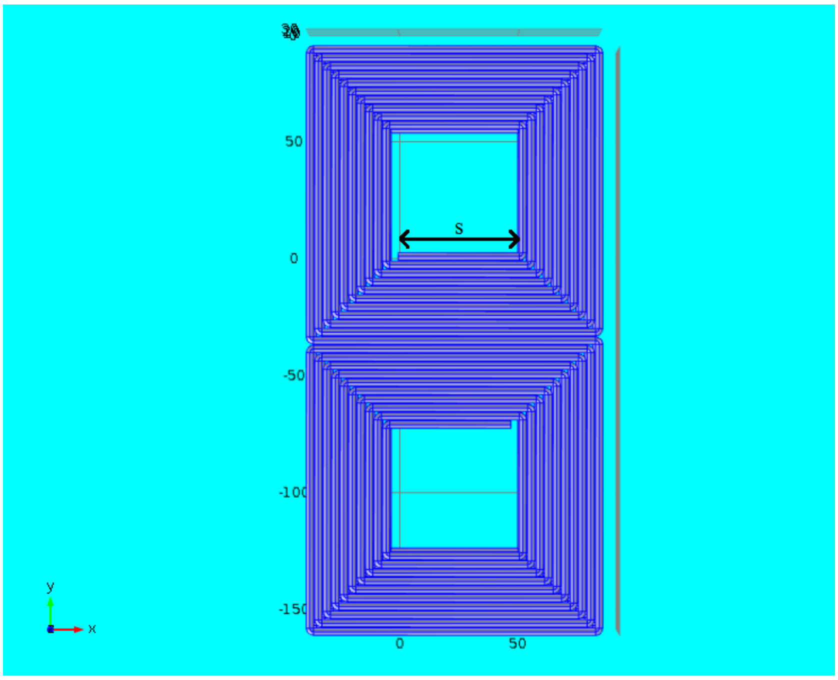

(b)

Fig. II.7. (a) 3D view of the DD coils; (b) x-y plane view of the DD coils

The results in terms of self-inductance L and mutual inductance M of the investigated structures, as obtained from post-processing elaboration, are gained.

In Tab. II.5 the self-inductances L, the lengths l of each coil and the corresponding resistances $R_{ohm}$ are reported.

Each $R_{ohm}$ is gained according to the second Ohm law, that is (II.2), concerning a copper conductor whose length is l, whose section area is A and whose resistivity is $\rho_{Cu}$, that is $1.68 \cdot 10^{-8}\ \Omega \cdot m$.

The section area corresponds to the area of a circle whose diameter is 3 mm.

In Fig. II.8 the results in terms of mutual inductance are plotted with respect to the distance on the z axis and to the misalignment between the coils in the x-y plane. Yellow, blue and red colors correspond to an air gap width of 1 cm, 2 cm and 3 cm respectively.

For each color, the graduating shading refers to the changes of M with respect to the misalignment in the x-y plane, as highlighted by the color legends.

**TABLE II.5.**

FEATURES OF THE SINGLE COILS

| **Parameter** | **circular coils** | **DD coils (s = 4 cm)** | **DD coils (s = 5 cm)** | **DD coils (s = 6 cm)** |
|---|---|---|---|---|
| L [μH] | 13 | 20.69 | 24.56 | 29.47 |
| l [m] | 3.4 | 6.01 | 6.8 | 7.59 |
| $R_{ohm}$ [mΩ] | 8.1 | 14.3 | 16.2 | 18 |

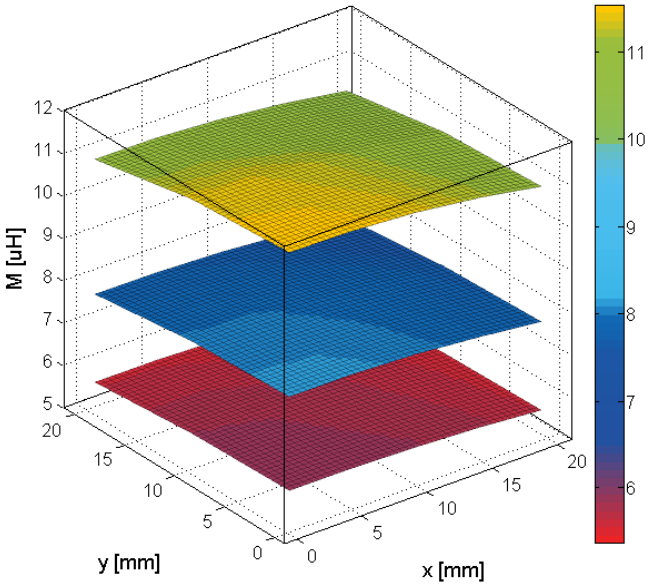
M [uH]
12
11
10
9
8
7
6
5
20
15
10
5
0
y [mm]
0
5
10
15
20
x [mm]
11
10
9
8
7
6

(a)

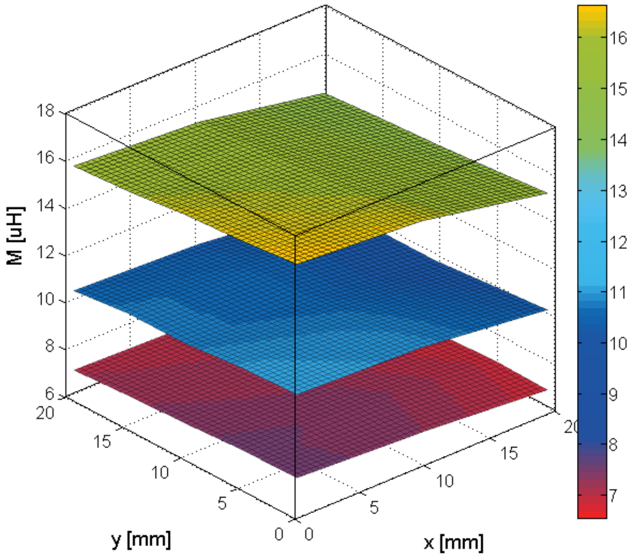
M [uH]
18
16
14
12
10
8
6
20
15
10
5
0
y [mm]
0
5
10
15
20
x [mm]
16
15
14
13
12
11
10
9
8
7

(b)

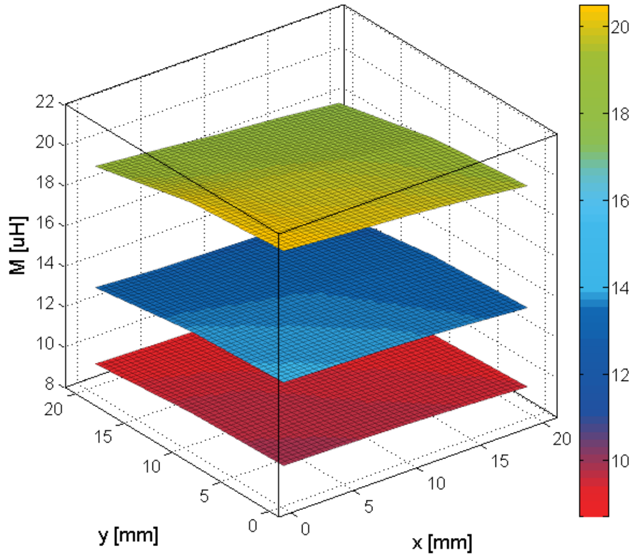

(c)

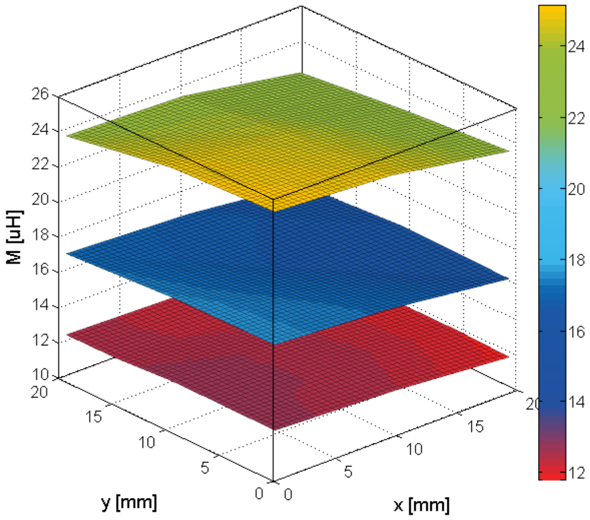

(d)

Fig. II.8. Mutual inductance M versus misalignments in the x-y plane for three different values of air gap in the z axis (yellow: 1 cm; blue: 2 cm; red: 3 cm) and for the 4 different structures: (a) circular coils; (b) DD coils (s=4 cm); (c) DD coils (s=5 cm); (d) DD coils (s=6 cm)

From an accurate analysis of the data, the best option in terms of tolerance to misalignments is the last one, that is represented by the DD coils with s = 6 cm. Indeed, for this option, the variation of M along both the x and y axes is comparable to the circular coils, and focusing only on the y axis, it turns out to be nearly null, as shown from Tab. II.6.

For each structure the percent variations of M are reported, concerning the maximal tested misalignments (2 cm) on the x and the y axes with respect to the perfect alignment (x = 0 ; y = 0).

The proposed options of inductive coupling structure are evaluated in terms of efficiency, considering different values of air gap width between the coils, and the system operating frequency is chosen accordingly. In the expressions (II.15) the terms $R_1$ and $R_2$ represent the primary and secondary power losses, including both the coil conduction losses and the MOSFETs conduction and switching losses. Supposing to use litz wires to build the inductively coupled coils, the skin effect can be neglected, so that the only contribution to the coil losses is the ohmic one, represented by $R_{ohm}$. Therefore, the term $R_{ohm}$ is included inside $R_1$ and $R_2$.

TABLE II.6.

PERCENT VARIATIONS OF M VERSUS THE MISALIGNMENTS

| **M var_% circular coils** | **x = 2 cm y = 0 cm** | **x = 0 cm y = 2 cm** | **x = 2 cm y = 2cm** |
|---|---|---|---|
| **z = 1 cm** | 5.63 | 5.39 | 10.47 |
| **z = 2 cm** | 5.21 | 4.92 | 9.91 |
| **z = 3 cm** | 4.74 | 4.55 | 9.22 |
| **M var_% DD coils (s = 4 cm)** | **x = 2 cm y = 0 cm** | **x = 0 cm y = 2 cm** | **x = 2 cm y = 2cm** |
| **z = 1 cm** | 8.77 | 5.35 | 13.66 |
| **z = 2 cm** | 7.73 | 5.85 | 13.89 |
| **z = 3 cm** | 9.59 | 6.37 | 14.14 |
| **M var_% DD coils (s = 5 cm)** | **x = 2 cm y = 0 cm** | **x = 0 cm y = 2 cm** | **x = 2 cm y = 2cm** |
| **z = 1 cm** | 7.32 | 5.54 | 13.38 |
| **z = 2 cm** | 7.01 | 4.6 | 11.72 |
| **z = 3 cm** | 6.43 | 4.31 | 11.87 |
| **M var_%** | **x = 2 cm** | **x = 0 cm** | **x = 2 cm** |

| **DD coils (s = 6 cm)** | **y = 0 cm** | **y = 2 cm** | **y = 2cm** |
|---|---|---|---|
| **z = 1 cm** | 6.33 | 5.54 | 11.19 |
| **z = 2 cm** | 7.18 | 2.75 | 9.12 |
| **z = 3 cm** | 6.67 | 1.79 | 7.36 |

The efficiency of the system is plotted versus the frequency and shown in Fig. II.9, for the following values of the distance between the coils respectively: 1 cm, 2 cm, 3 cm. No misalignment in the x-y plane is considered at this stage.

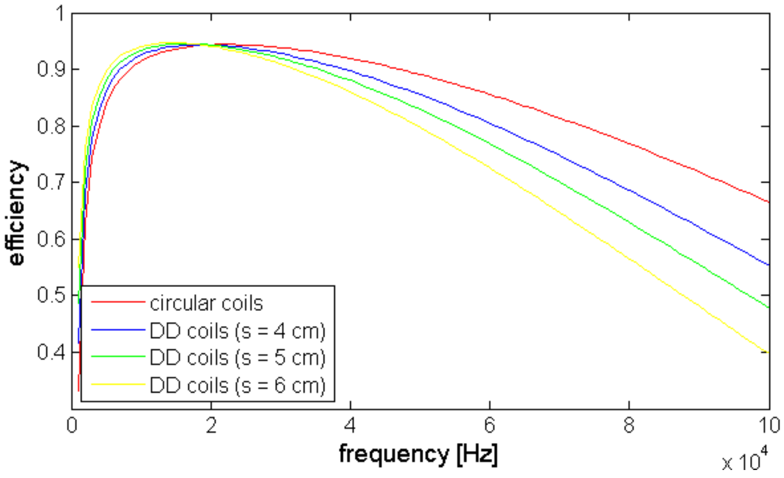

(a)

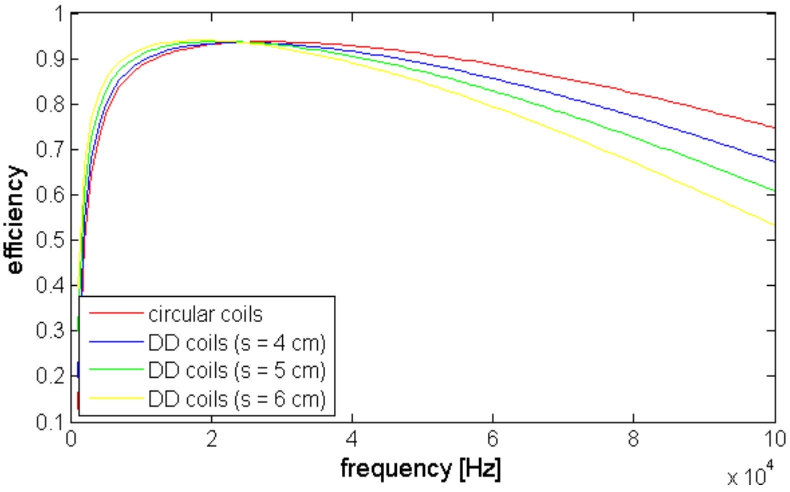

(b)

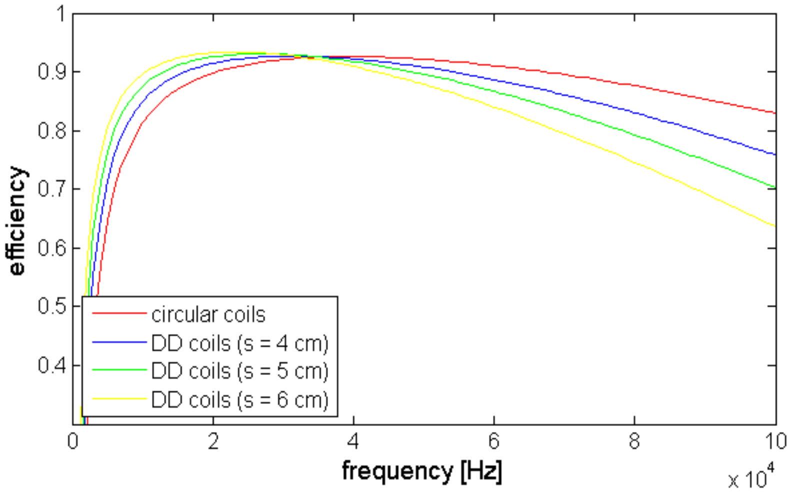

(c)

Fig. II.9. Efficiency versus frequency for three values of air gap width between the two coils: (a) 1 cm; (b) 2 cm; (c) 3 cm

The value of 30 kHz represents a good choice for the operating frequency, since at this frequency the 4 investigated structures roughly show the maximum efficiency. Therefore, the compensation capacitors shall be sized according to this frequency.

The last term of comparison among the investigated options concerns the effect on the power efficiency of the misalignment between the primary coil, connected to the grid, and the secondary coil, connected to the E-bike battery. Supposing that the primary coil lies on the support holding the bicycle up during the parking time and that the secondary coil lies on the front wheel of the bicycle, parallel to the primary, there could be a not perfect alignment between the coils with respect to a plane which is parallel to them (corresponding to the x-y plane), so that an investigation of the effects of this misalignment on the wireless power transfer efficiency can be useful. Fig. II.10 show the system efficiency, at the frequency of 30 kHz, with respect to the mutual inductance M.

The figures refer to different air gap widths: 1 cm, 2 cm and 3 cm respectively. For each figure, the efficiency is plotted with respect to four different discrete M slots. Each slot concerns each of the four investigated structures of inductive coupling and corresponds to the range of possible misalignments on the x-y plane, from 0 to 2 cm for both the axes. The behavior of M as function of the misalignments has been highlighted in Fig. II.8.

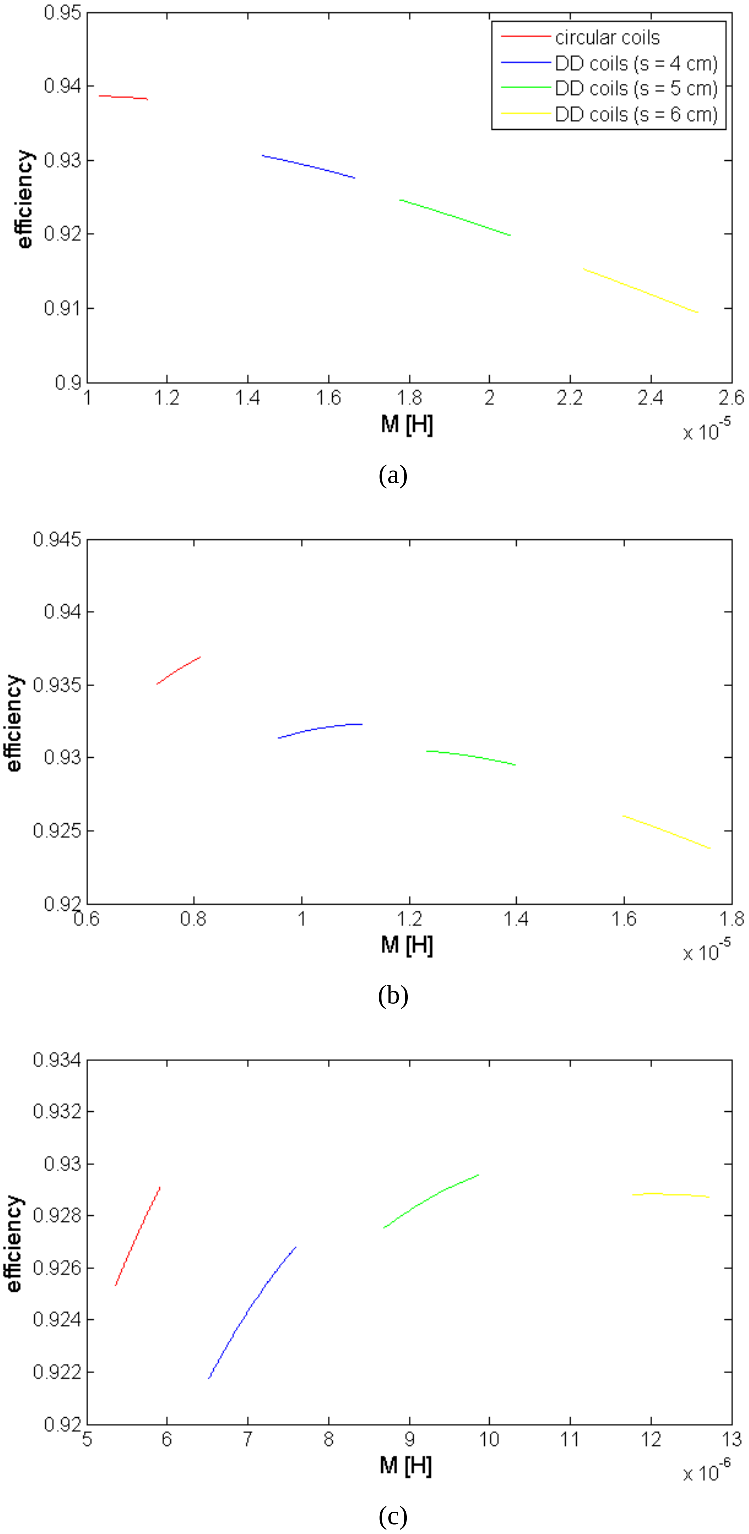

Fig. II.10. Efficiency versus the mutual inductance M, for three values of air gap width between the two coils: (a) 1 cm; (b) 2 cm; (c) 3 cm

As shown by the figures, the DD coils feature, especially for the highest distances between the coils, excellent tolerance to the misalignments in terms of effect on the system efficiency. Among the investigated DD coils, particularly the largest solution turns out to be extremely tolerant to the x-y misalignments.

## II.3. Control

A control action is required on the IPT system in order to regulate the power flow towards the E-bike battery. Although the control can be implemented in different ways according to the peculiar topologies that are employed, the common goal is to produce the desired output at the battery section.

As explained in Chapter I, the main stages of a typical lithium ion battery are the constant current stage and the constant voltage stage. The control action is therefore dependent on the specific stage of the battery charging process.

During the constant current stage, the goal is to keep the battery current fixed at a certain value, whereas during the constant voltage stage, the battery voltage needs to be kept fixed at a certain value. The compensation topology of the proposed IPT system is series-series (SS). The output of the SS topology is roughly equivalent to a current source at the resonant frequency, so that in this case the control is more easily effective during the constant current stage [70]. If a proper frequency is chosen as the system operating frequency, the SS output is equivalent to a voltage source, so that at this frequency the constant voltage stage is more easily controllable [70].

### II.3.1. Algorithm for the efficiency optimization

According to Fig. II.5 and to the values in Tab. II.4, the efficiency of the system has been studied as function of the phase control parameters, aiming at the implementation of an algorithm for the efficiency optimization. This work has been reported in [127] and [128].

The power efficiency is defined as:

$$\eta = \frac{P_2}{P_1} \tag{II.16}$$

The projections of the power efficiency η onto the ($\varphi_{S1}$ - $\varphi_{S2}$) plane are displayed in Fig. II.11 and Fig. II.12, according to (II.15) and (II.16). The contour lines of the battery power $P_2$ are shown as well, according to (II.15). Each contour line represents a constant power locus. The displayed contour lines represent power levels up to 200 W in Fig. II.11 and up to 160 W in Fig. II.12.

By representing different cases of resistances $R_1$ and $R_2$, the figures show that the maximum efficiency point for a specific power level is dependent upon the resistances. $R_1$ and $R_2$ are the equivalent resistances at the primary and at the secondary side.

Due to the dependence of the maximum efficiency on the specific system, featuring power losses which are not easy to be accurately calculated, an “on-line” algorithm aiming at the maximum efficiency point is proposed in order to lock the maximum efficiency point.

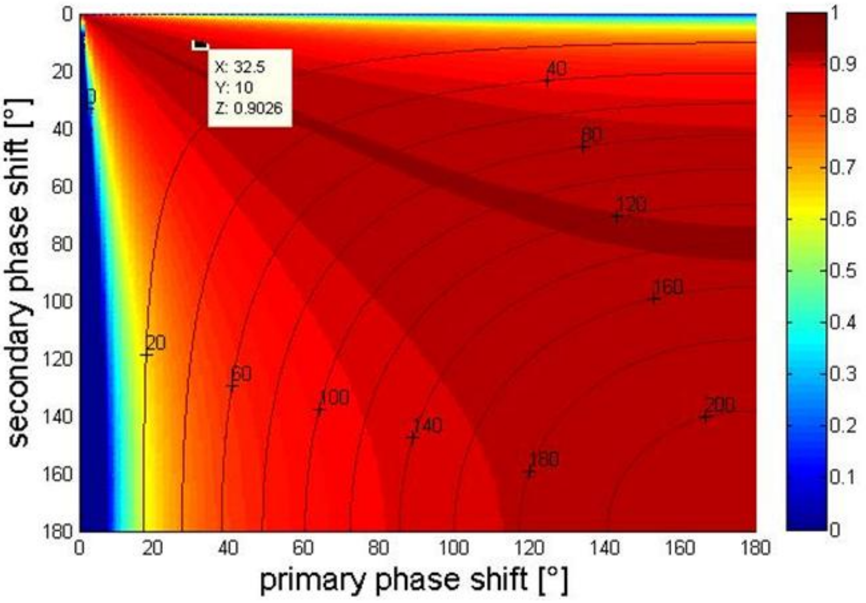

Fig. II.11. Color field referred to efficiency η and contour lines referred to power $P_2$ expressed in Watt, as functions of primary phase shift $\varphi_{S1}$ and secondary phase shift $\varphi_{S2}$:
$R_1 = R_2 = 0.125\ \Omega$

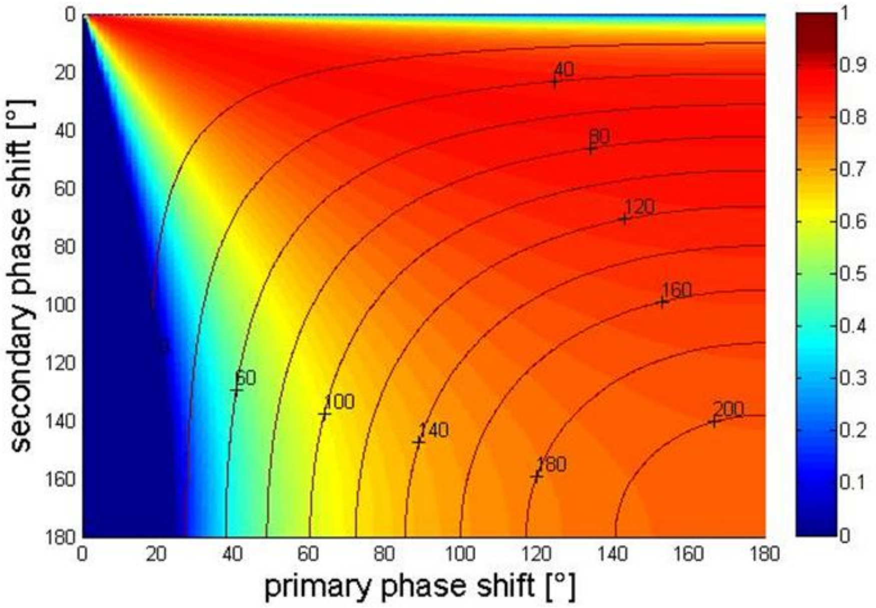

Fig. II.12.Color field referred to efficiency η and contour lines referred to power $P_2$ expressed in Watt, as functions of primary phase shift $\varphi_{S1}$ and secondary phase shift $\varphi_{S2}$:
$R_1 = 0.425\ \Omega$; $R_2 = 0.125\ \Omega$

This is an actual power tracking algorithm, based on a perturbation of two control variables, until the point of maximum efficiency is achieved and locked for the required power level. The algorithm is based on an actual “perturb and observe” method, as shown in Fig. II.13.

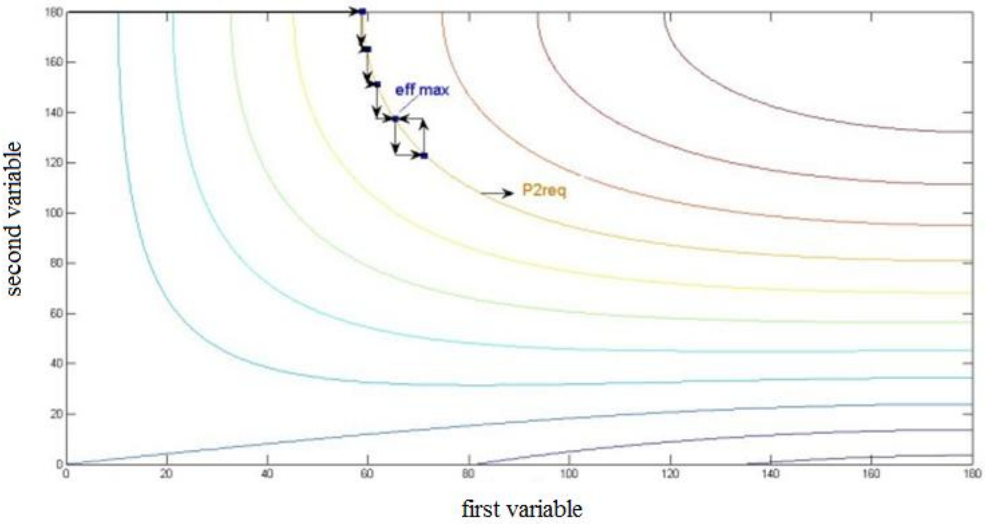

Fig. II.13.  Power tracking algorithm for the maximization of the efficiency

Periodically, the first variable is incremented step-by-step. When the required power level is sampled, the first variable is kept constant, while the other one is varied by a step. After that, the first variable is incremented again step-by-step, until the required power level is reached. Every time the power level is achieved, the efficiency is registered, until the maximum efficiency level is reached on that power level curve. After every step, it is necessary to wait a period of time in order to sample and hold the current power level, so that the system can have enough time to reach the steady state. The sample period is chosen equal to 10 ms, whereas the waiting time after every step is 7.5 ms. The algorithm has been implemented through simulations, carried out by *PowerSIM* [125]. The two control variables are the phase delay $\varphi_D$ and the phase shift $\varphi_S$ concerning the phase difference between $V_2$ and $V_1$ and the full-bridge phase shift in the system of Fig. II.14, where a half-bridge transmitter is used. Even if the maximum efficiency occurs for $\varphi_D$ equal to 90°, thus making a 2-variable algorithm useless, the correctness of the implemented algorithm has been validated through the comparison between the simulation results and the analytical model in terms of maximum efficiency level and maximum efficiency point. Fig. II.15 shows the valuable waveforms of the power tracking algorithm: phase delay, phase shift and $V_{sample}$, which is the voltage obtained by sensing, sampling and holding the battery current.

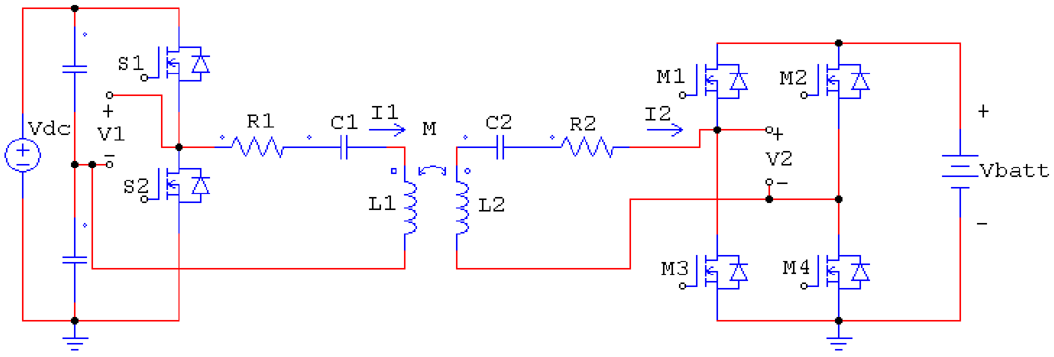

Fig. II.14. Model of an IPT system with a half-bridge in the primary side and a full-bridge in the secondary side

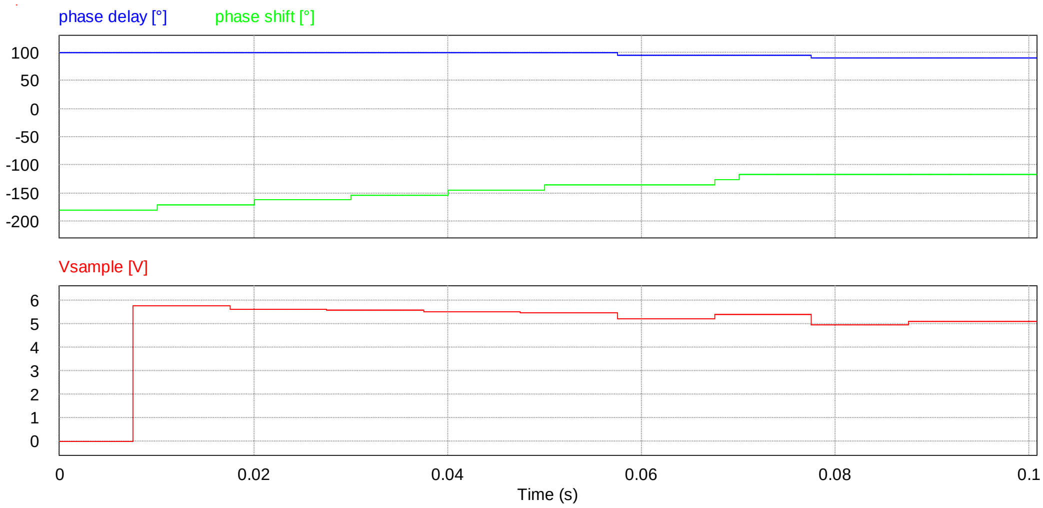

Fig. II.15. Phase shift, phase delay and $V_{sample}$ during the power tracking algorithm for efficiency optimization

Every 10 ms the phase shift is incremented by 9°, whereas the phase delay is incremented by 5° every time the required power level is reached. By reducing the angle steps for the two control variables, the algorithm would be more precise, tending to the actual power curve in the ($\varphi_D$ – $\varphi_S$) plane. In this specific example the phase shift starts to be spanned from 0° and the phase delay from 80°.The figure shows that the maximum efficiency is locked, at a 90° phase delay, coherently with the analytical results. The reference battery current is 5 A.

In this Chapter an IPT system for E-bike battery charging has been proposed. The power level ranges from 100 W to 250 W and the considered load is a 36 V 10 Ah $LiFePO_4$ battery.

After a detailed description of the magnetic and electronic design procedure, an alternative IPT system, useful for a Bi-Directional power transfer, has been analyzed. The power and the efficiency as functions of some control parameters, such as the phase delay and the phase shift, have been gained. The mathematical model has been validated through electronic simulations.

Based on this mathematical study, an algorithm for the efficiency optimization has been proposed and the simulation results have been shown in order to demonstrate its correctness and validity.

Alternative options of inductively coupled coils have been investigated and compared to the assembled coils, in order to evaluate the best solution as far as system efficiency and tolerance to misalignments between the coils are concerned.

The investigation has been carried out through a 3D magnetic simulator and different cases of air gap width between the coils have been considered as well.

In Chapter III the experimental prototype will be shown. The results in terms of power efficiency and magnetic flux density in the region surrounding the working system will be provided.

# Chapter III

# Experimental prototype and measurements

A laboratory prototype of an IPT system has been assembled, according to the schematic shown in Fig. III.1.

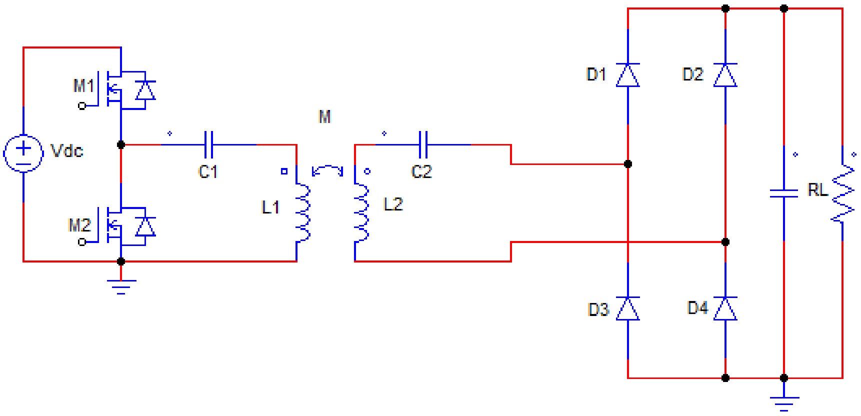

Fig. III.1. Schematic of the assembled IPT prototype

$V_{dc}$ represents the DC output of the grid-connected AC-DC stage. The load resistance $R_L$ represents the input of the battery charging control network. In the power transmitter side, the DC-AC is implemented through a half-bridge inverter, including the nMOS M1 and M2. In the power receiver subsystem, a conventional four-diode rectifier is employed (D1-D2-D3-D4). In order to reduce power losses, Schottky diodes are used. The IPT is modelled by $L_1$, $L_2$ and M. $L_1$ and $L_2$ are the primary and the secondary self-inductances respectively; M is the mutual inductance, linked to the self-inductances and the coupling coefficient k according to (II.1); $C_1$ and $C_2$ are the series capacitors of the compensation topology, required to maximize the amount of transferred power and to minimize the reactive power drawn by the electrical grid.

System working, power transfer efficiency and produced magnetic field of the assembled prototype have been evaluated according to different operating conditions, as explained in the next paragraphs.

## III.1. Practical implementation

For the designed IPT system a laboratory prototype has been assembled and several experimental tests have been carried out to test the proper working and to measure the power efficiency and the produced magnetic field. The application target for this prototype corresponds to a (100÷250) W power range, useful for the charging of an electric bicycle battery. In the next subparagraphs, the different parts of the assembled IPT prototype will be described.

### III.1.1. Winding coils

The Inductive Power Transfer is implemented through the magnetic coupling between two coils. For the experimental prototype, two circular coils have been used, whose features are listed in Tab. II.1 and Tab. II.2 and again reported in Tab. III.1 and Tab. III.2:

**TABLE III.1.**

CHARACTERISTICS OF THE PROPOSED COUPLING STRUCTURE

| **Material** | **Value** |
|---|---|
| $\rho_{Cu}$ | $1.68 \cdot 10^{-8}\ \Omega \cdot m$ |
| $\mu_{r,Cu}$ | ~1 |
| **Wire geometry** | **Value** |
| d | 3 mm |
| l | 3.48 m |
| **Coil geometry** | **Value** |
| $d_{out}$ | 15 cm |
| N | 9 |
| maximum air gap | 3 cm |

**TABLE III.2.**

ELECTRIC CHARACTERIZATION OF THE PROPOSED COUPLING STRUCTURE

| **Element** | **Value** |
|---|---|
| $L_1 = L_2 = L$ | 13 µH |
| M | 4.9 µH |
| k | 0.377 |
| $R_{dc}$ | 8.2 mΩ |

The realized coils are shown in Fig. III.2.

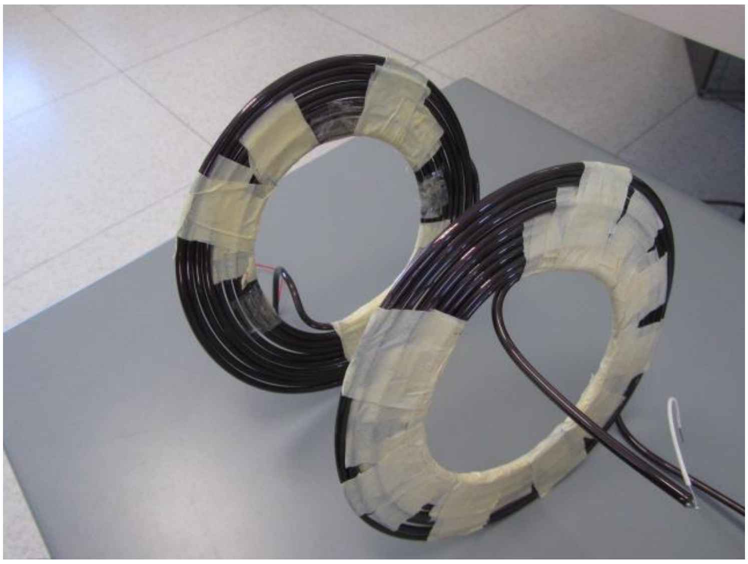

Fig. III.2. Photograph of the assembled coils

### III.1.2. Compensation capacitances

The series capacitances $C_1$ and $C_2$ are practically implemented through two sets of capacitors. Each set includes nine capacitors, in order to reduce voltage and current across the single components, considering that the system potentially works at the resonant frequency. For each set, the 9 capacitors consist of three groups of parallel-connected capacitors; these three groups are series-connected.

As explained in Chapter II, the chosen theoretical resonant frequency is 100 kHz. According to the 100 kHz resonant frequency and the 13 µH self-inductances, the compensation capacitors $C_1$ and $C_2$ should be equal to 194.8 nF, arising from (II.3). Considering that the closest commercial value for capacitances is 220 nF, the real resonant frequency is exactly equal to 94.1kHz, according to (II.3) and considering both the primary and secondary resonant frequencies equal to the operation resonant frequency.

In order to obtain a total capacitance of 220 nF for each set, each of the 9 capacitances has to be equal to 220 nF as well. The following capacitors have been selected for the assembled prototype [131]:

- power transmitter stage:
  capacitance: 220 nF; max voltage: 1250 V; producer: *Epcos*;
- power receiver stage:
  capacitance: 220 nF; max voltage: 630 V; producer: *Epcos*.

### III.1.3. Power electronics

For the realization of the experimental prototype, the power electronics components in both the transmitter and the receiver stage have been accurately chosen, according to the simulation model whose schematic is shown in Fig. III.1.

The schematic shown in Fig. III.3 describes the actual components in the transmitter stage of the prototype.

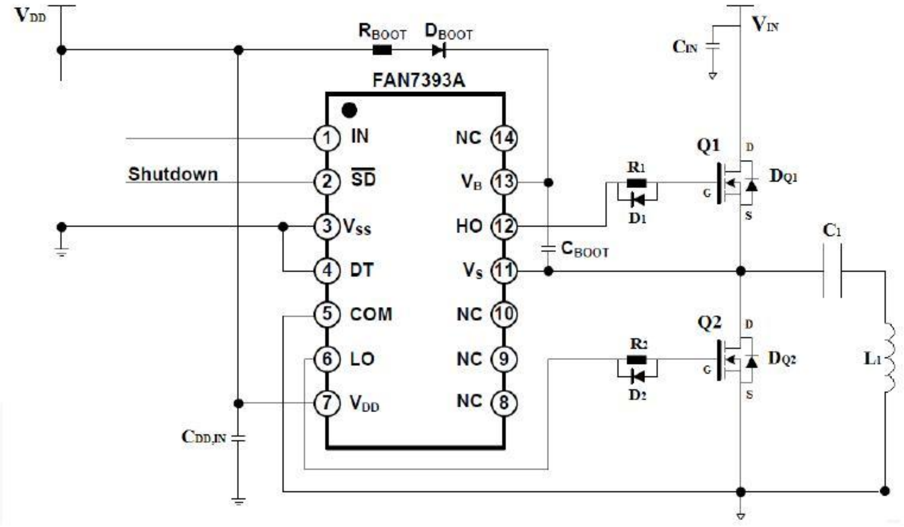

Fig. III.3. Schematic of the realized transmitter board

The half-bridge (nMOS Q1-Q2) is shown together with the electronic network useful for the active elements driving, which has not been given in detail in the simulation model of Fig. III.1.

The half-bridge control network consists of a MOSFET driver and of a bootstrap circuit. According to Fig. III.3, the driver is the component *FAN7393A*, by *Fairchild Semiconductor* [132]. The pin configuration is shown as well. The driver is used to produce the proper amounts of gate currents to switch both the MOSFETs Q1 and Q2, according to a square wave input signal applied to the pin IN. The bootstrap network, consisting of the resistor $R_{BOOT}$ and of the diode $D_{BOOT}$, is a passive circuit useful to turn correctly on the high-side MOS (Q1), whose source potential is floating.

The components in the transmitter stage are the following:

- half-bridge driver: *FAN7393A*, *Fairchild Semiconductor*;
- nMOSFETs in half-bridge configuration (Q1-Q2): *STB120NF10T4*, *STMicroelectronics* [133];
- boostrap diode ($D_{BOOT}$): *VS-11DQ09*, Schottky, 1.1 A, 90 V, *Vishay* [134];
- bootstrap resistor ($R_{BOOT}$): 2.2 Ω, 5%, 3 W, *Vishay*;
- bootstrap capacitor ($C_{BOOT}$): 0.47 µF, 50 V, *Panasonic* [135];
- capacitor in parallel with the $V_{IN}$ half-bridge supply ($C_{IN}$): 6.8 mF, 100 V, *Panasonic*;
- capacitor in parallel with the $V_{DD}$ bootstrap circuit supply ($C_{DD,IN}$): 0.47 µF, 50 V, *Panasonic*;
- resistors in series with the MOS gates ($R_1$-$R_2$): 10 Ω, 5%, 3 W, *Vishay*;
- diodes in parallel with the resistor $R_1$ and $R_2$ ($D_1D_2$): *VS-11DQ09*, Schottky, 1.1 A, 90 V, *Vishay*;
- diodes in parallel with the MOSFETs ($D_{Q1}$-$D_{Q2}$): *SS3H9*, Schottky, 3 A, 90 V, *Vishay*.

In the receiver stage, a conventional 4-diode rectifier has been assembled. The diodes and the capacitors at the rectifier output are the following:

- diodes: *SS3H9*, Schottky, 3 A, 90 V, *Vishay*;
- capacitors: 10 µF, 100 V, *Epcos*.

## III.2. Layout design

The layouts of the printed circuit boards for the transmitter stage and for the receiver stage have been designed through the software [136].

In the Fig. III.4 and Fig. III.5 the transmitter stage layout and the receiver stage layout are respectively shown. The red areas refer to the top part, whereas the blue areas refer to the bottom part of the printed circuit boards.

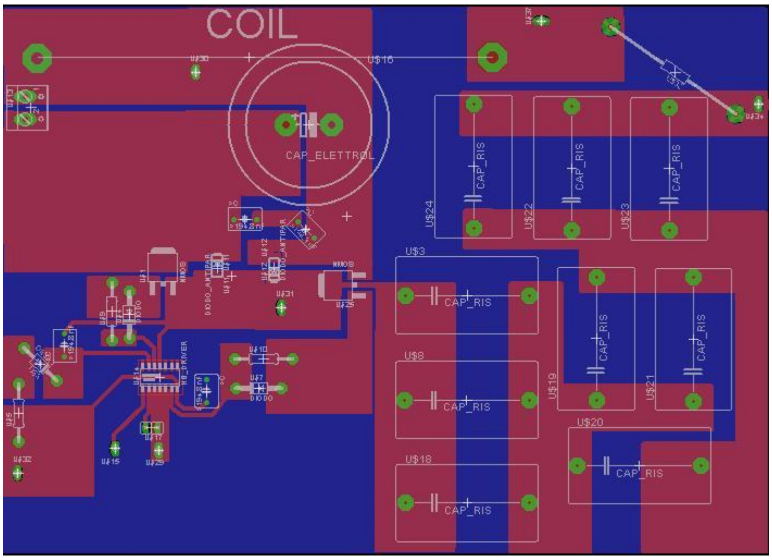

Fig. III.4. Layout of the power transmitter board

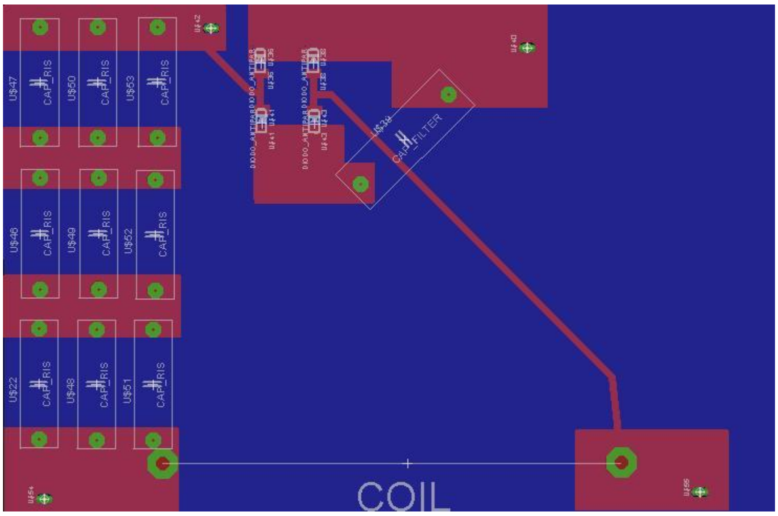

Fig. III.5. Layout of the power receiver board

## III.3. Experimental setup

In Fig. III.6 the prototype of the designed IPT system for E-bike battery charging is shown. For the assembled system several experimental tests have been carried out to test the proper working and to measure the power efficiency and the magnetic field. Power transmitter side and power receiver side are built on the printed circuit boards on the left and on the right of the figure respectively, and they are respectively connected to the primary coil and to the secondary coil.

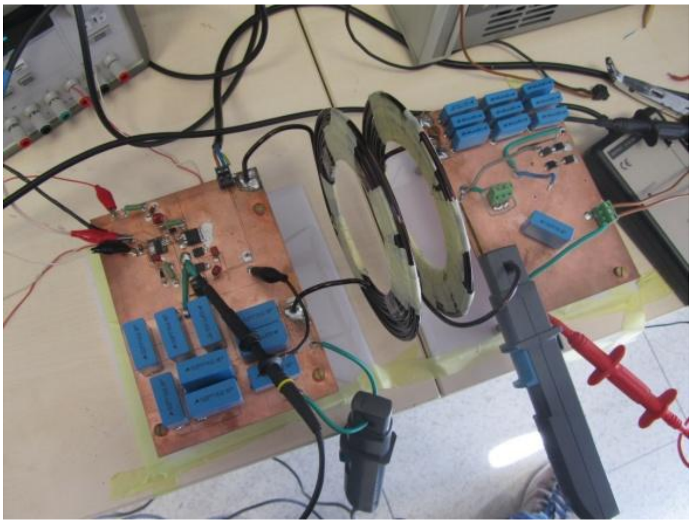

Fig. III.6. The assembled prototype of the proposed IPT system

A test bench has been set up at its schematic representation is shown in Fig. III.7. In addition to the electronic boards, the bench is composed by the following components:

- a DC voltage source, which is used to supply the half-bridge and the MOSFET drivers of the transmitter board;
- a function generator which is used to produce the AC waveform driving the MOSFETS, in order to power the primary coil;
- an electrical load, representing $R_L$ according to Fig. III.1 and consisting in an electronic load or in a rheostat, depending on the type of measurements;

- a measuring system composed by two voltmeters connected to the terminals of the coils and two current probes, used for the current measurement of both coils;
- a power scope, which is used for the real-time waveform detection and measurement of the main electrical quantities involved in the proposed system;
- a magnetic probe for the magnetic field characterization of the system.

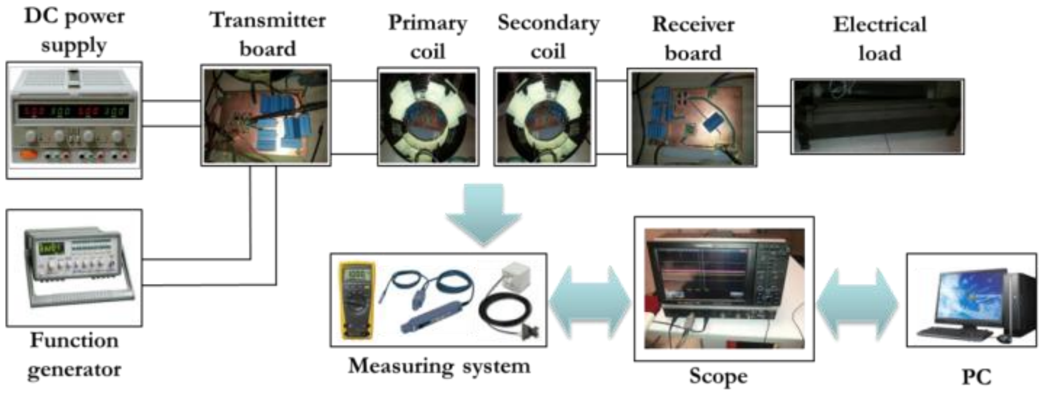

Fig. III.7. Schematic representation of the whole test bench

## III.4. Electrical measurements

The measurements have been done setting a 2 A electronic load and in open-loop configuration. The proper working of the system, evaluated at the resonance frequency, is highlighted by the similarity between the waveforms resulting from the experimental tests and the ones resulting from the simulation tests. As envisioned in the design phase, a 3 cm air gap between transmitter and receiver coils has been set.

Fig. III.8 displays the waveforms referring to voltage and current under resonance on primary and secondary sides, for a 24.2 V supply.

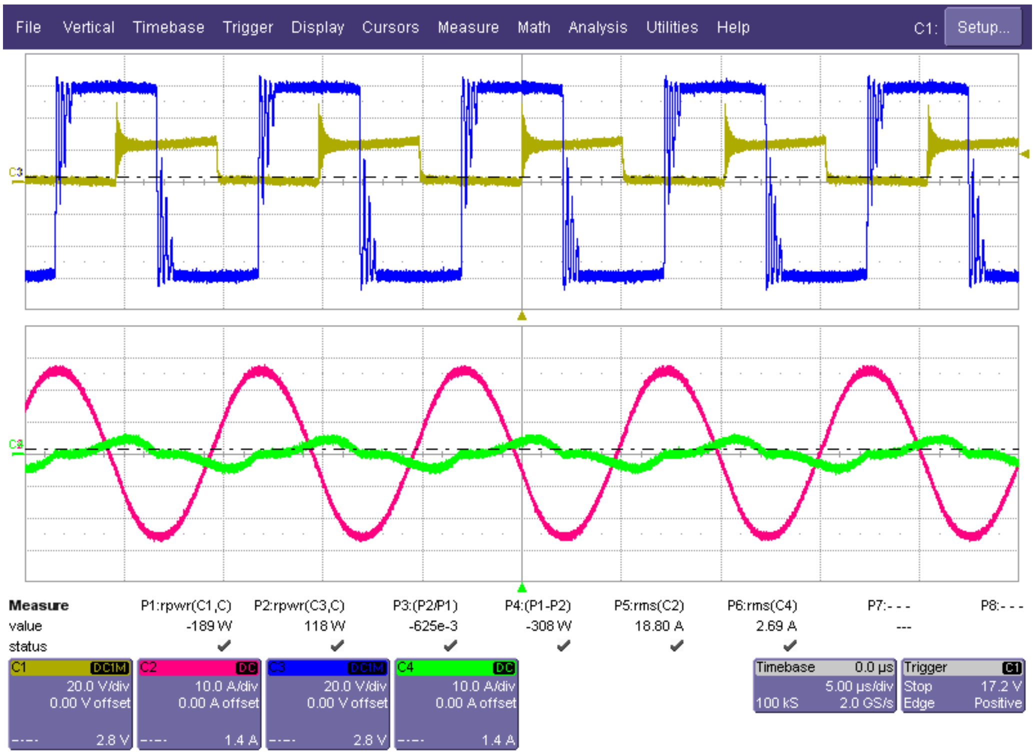

| Measure | P1:rpwr(C1,C) | P2:rpwr(C3,C) | P3:(P2/P1) | P4:(P1-P2) | P5:rms(C2) | P6:rms(C4) | P7:- - - | P8:- - - |
|---|---|---|---|---|---|---|---|---|
| value | -189 W | 118 W | -625e-3 | -308 W | 18.80 A | 2.69 A | --- | |
| status | ✓ | ✓ | ✓ | ✓ | ✓ | ✓ | | |

C1 DC1M 20.0 V/div 0.00 V offset 2.8 V

C2 DC 10.0 A/div 0.00 A offset 1.4 A

C3 DC1M 20.0 V/div 0.00 V offset 2.8 V

C4 DC 10.0 A/div 0.00 A offset 1.4 A

Timebase 0.0 µs 5.00 µs/div 100 kS 2.0 GS/s

Trigger C1 Stop 17.2 V Edge Positive

Fig. III.8. Waveforms of voltage and current measured under resonance

Horizontal axis is set with a 5 µs/div time division. C1 and C3 channels display the measured voltages with a 20V/div voltage division, whereas C2 and C4 display the currents with a 10A/div current division. C1 refers to the primary voltage, $V_1$ (that is the voltage of the phase node in the half-bridge); C3 refers to the secondary voltage, $V_2$ (that is the voltage at the input of the rectifier). C2 refers to the primary current, $I_1$; C4 refers to the secondary current, $I_2$.

After that, different measurements at different working conditions have been made.

Post-processing calculations referring to real input and output powers of the magnetic coupling network, referenced as P1 and P2 respectively, and to the coupling efficiency $\eta_{coup}$, referenced as P3, have been made by the oscilloscope. The real primary power is the real power associated to the product between $V_1$and $I_1$, while the real secondary power is the real power corresponding to the product between $V_2$ and $I_2$. The coupling efficiency is the $P_2/P_1$ ratio, whereas the overall efficiency is the $P_{out}/P_{in}$ ratio, where $P_{out}$ is the power on the load and $P_{in}$ is the source power. Therefore, the following expressions arise:

$$\begin{aligned} P_1 &= \overline{V_1 I_1} \\ P_2 &= \overline{V_2 I_2} \\ \eta_{coup} &= \frac{P_2}{P_1} \\ \eta &= \frac{P_{out}}{P_{in}} \end{aligned} \tag{III.1}$$

Fig. III.9 shows both input and output AC power curves (that are $P_1$ and $P_2$) versus frequency under a 20 V primary supply $V_{dc}$. The maximum measured power in this operating conditions is equal to 91 W. The gained experimental data about the power efficiency have been collected into two graphics: the first one by fixing the supply voltage and varying the operating frequency; the second one by fixing the operating frequency and varying the supply voltage.

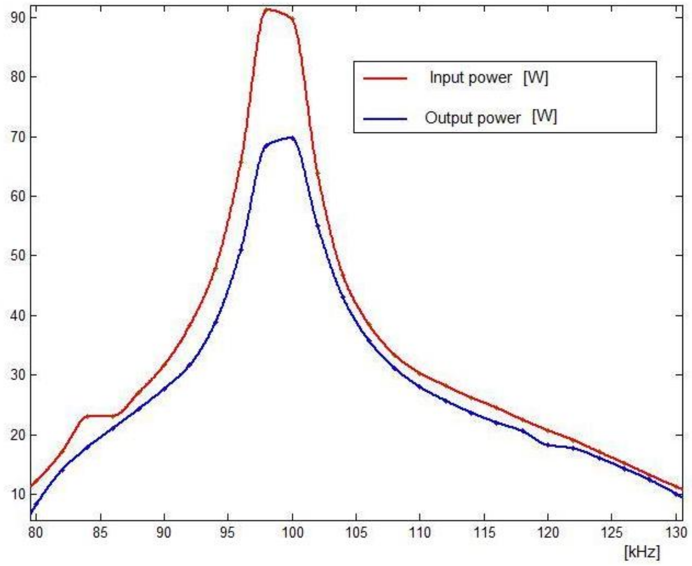

Fig. III.9. Measured input and output AC power versus operating frequency under a 20 V primary supply

In Fig. III.10 the first set of data is shown. Both coupling and overall efficiency curves versus operating frequency are displayed, as obtained from experimental data. The experimental measurements have been performed with a 2 kHz frequency step and the acquired data points have been plotted through a third degree polynomial fitting.

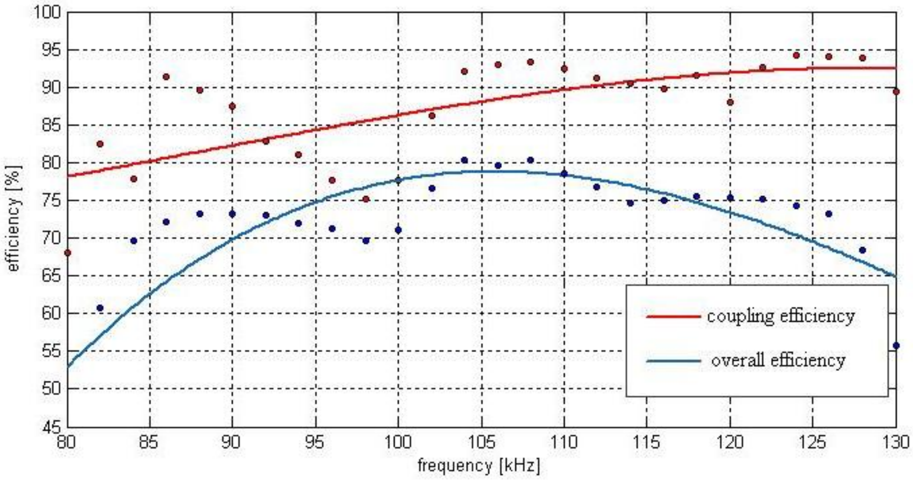

Fig. III.10. Experimental efficiency curves versus operating frequency under a 20 V supply voltage

Considering the rectifier power losses, the overall efficiency is obviously less than the coupling efficiency. The coupling efficiency increases in the starting part of the (80÷130) kHz range whereas it keeps constant for the highest frequencies, due to the increasing skin effect contribution. The overall efficiency decreases for the highest frequencies due to the increasing switching losses inside the rectifier. A 94% maximum coupling efficiency is experimentally measured for a 17 W power transfer at 124 kHz. The maximum overall efficiency is obtained at 104 kHz, and for this frequency Fig. III.11 shows the second set of data, referring to the measured coupling efficiency by varying the supply voltage.

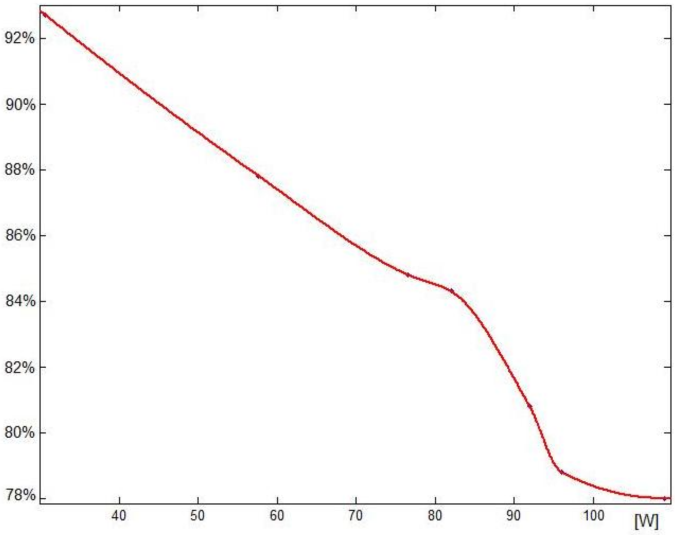

Fig. III.11. Coupling efficiency curve versus load power at 104 kHz

By increasing the supply voltage, the efficiency decreases due to the coil conduction losses because of the increase in current. At a supply voltage of 46 V, the output DC power is the desired one, that is 96 W. For this power, the coupling efficiency is 79%.

## III.5. Magnetic measurements

A magnetic characterization of the region surrounding the working system has been carried out, through the measurement of the magnetic flux density in different points and for three different values of distance between the coils: 1 cm, 2 cm and 3 cm. The goal of the magnetic measurements has mainly been the evaluation of the conditions for which the guidelines concerning the exposure of the human body to the electromagnetic fields are satisfied, with respect to the proposed IPT system. [137] has resulted from this work, described in the following.

### III.5.1. Physiological compatibility of the IPT for E-bikes

Although the wireless battery charging provides benefits in terms of human safety, not implying electrocution risks arising from the plug-in operation, some concern should be addressed to the magnetic field exposure due to the IPT-based operation. In scientific literature, although few works report the simulation results concerning the magnetic field distribution in wireless charging of electric cars and bicycles, no experimental result has been reported yet [27].

Accurate considerations on the potential risks arising from the magnetic field in a wireless charger for electric vehicles strongly depend on the typology of the investigated vehicles. For instance, the electric car and the E-bike represent two inherently different case studies as far as an IPT-based wireless battery charging is concerned. In the case of the car, the metal chassis of the vehicle protects the passengers from the magnetic field exposure. Most of the magnetic energy is contained inside the narrow gap between the road and the car, where the transmitter and the receiver coil are respectively placed [94]. In spite of the high power levels involved, the wireless charging operation turns out to be quite safe.

Due to the lower power levels, the magnetic fields produced by IPT are supposed to be weaker in the E-bike case in comparison with the car case. Nevertheless, the human exposure to the magnetic field is potentially more likely, as the cyclist is not protected by a chassis like in the case of the car. Furthermore, supposing a scenario where different electric bicycles are parked next to the sidewalk and being inductively charged, the pedestrians or other cyclists could be exposed to the magnetic radiation. To evaluate the effect of the produced magnetic field on the human body, the guidelines of ICNIRP have been considered. In Fig. III.12 the ICNIRP guidelines concerning the general public exposure are highlighted [116].

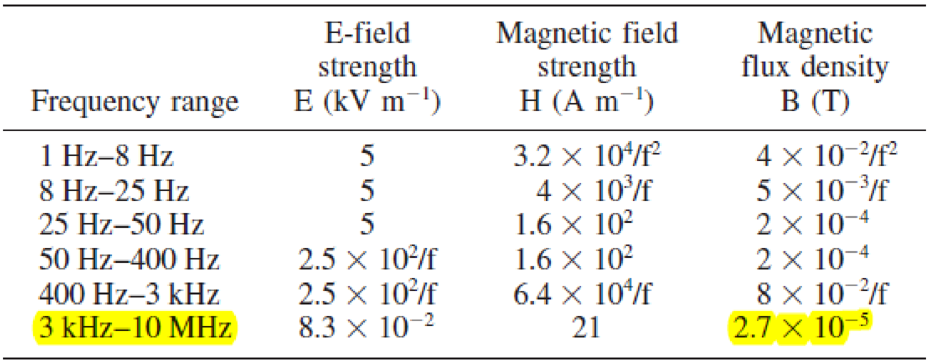

| Frequency range | E-field strength E ($kV\ m^{-1}$) | Magnetic field strength H ($A\ m^{-1}$) | Magnetic flux density B (T) |
|---|---|---|---|
| 1 Hz–8 Hz | 5 | $3.2 \times 10^4/f^2$ | $4 \times 10^{-2}/f^2$ |
| 8 Hz–25 Hz | 5 | $4 \times 10^3/f$ | $5 \times 10^{-3}/f$ |
| 25 Hz–50 Hz | 5 | $1.6 \times 10^2$ | $2 \times 10^{-4}$ |
| 50 Hz–400 Hz | $2.5 \times 10^2/f$ | $1.6 \times 10^2$ | $2 \times 10^{-4}$ |
| 400 Hz–3 kHz | $2.5 \times 10^2/f$ | $6.4 \times 10^4/f$ | $8 \times 10^{-2}/f$ |
| 3 kHz–10 MHz | $8.3 \times 10^{-2}$ | 21 | $2.7 \times 10^{-5}$ |

Fig. III.12. ICNIRP guidelines concerning the general public exposure:
the limit for the magnetic flux density is highlighted for the IPT frequencies

In order to investigate the distribution and the strength of the magnetic field and to understand the safety distance from the charging system, several simulations and experimental tests have been carried out. The tested object is represented by the assembled prototype of IPT system for E-bike charging, consisting of the two flat and circular coils as the main part as far as magnetic field production is concerned. In Tab. III.3 the electrical features of the IPT system are provided for the magnetic characterization of the system.

$R_L$ has been implemented by a rheostat. A 100 W load power has been chosen.

TABLE III.3.

ELECTRICAL FEATURES OF THE IPT PROTOTYPE
FOR THE MAGNETIC FIELD ESTIMATION

| Element | Value |
|---|---|
| **$L_1 = L_2 = L$** | 13 µH |
| **M (air gap)** | 9.6 µH (1 cm) |
| | 6.6 µH (2 cm) |
| | 4.9 µH (3 cm) |
| **$C_1 = C_2 = C$** | 220 nF |
| **$R_L$** | 7 Ω |

According to ICNIRP guidelines, as shown by Fig. III.12, the rms value of magnetic flux density $|B_{rms}|$ which should be considered as the maximum limit for general public exposure is 27 µT at the frequency of 94.1 kHz. Since both the magnetic simulation tool and the measuring instrument provide peak values, the reference limit, according to ICNIRP, is 38 µT according to the following expression:

$$|B| = \sqrt{2} \cdot |B_{rms}| \qquad \text{(III.2)}$$

where |B| is the peak value of the magnetic flux density.

### III.5.1.1. Magnetic simulations

Simulation tests in order to obtain the magnetic flux density around the proposed coupling structure have been carried out through a 2D FEM-based software [124]. Fig. III.13 refer to three different values of width of the air gap between the transmitter coil and the receiver coil: 1 cm, 2 cm and 3 cm. The figures show a cross section of the structure. The left edge of the image corresponds to the axis of the imaginary cylinder whose bases are the circular planes belonging to the coils.

According to a 100 W power on the load resistor, the currents flowing on the primary and the secondary self-inductances have been evaluated through a power electronics simulation software [125] and simulated on the coils in the FEM software. The resulting magnetic flux density is higlighted in the figures.

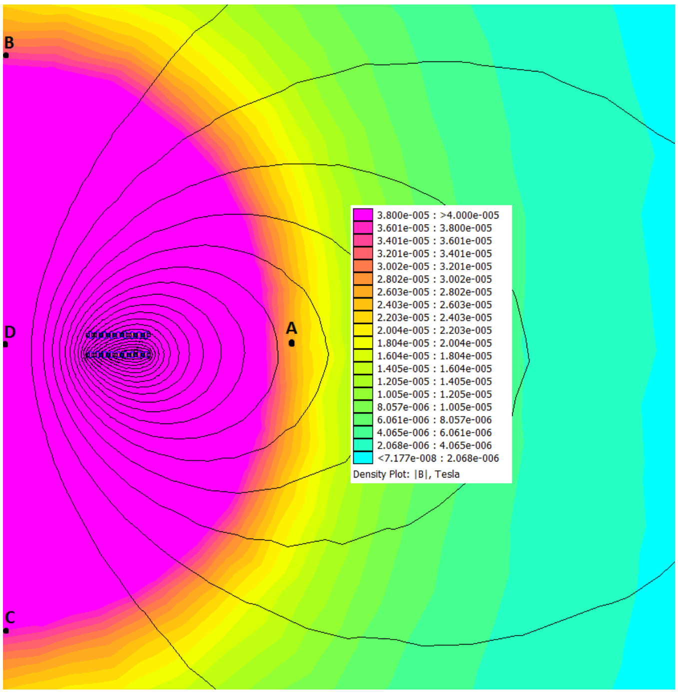

(a)

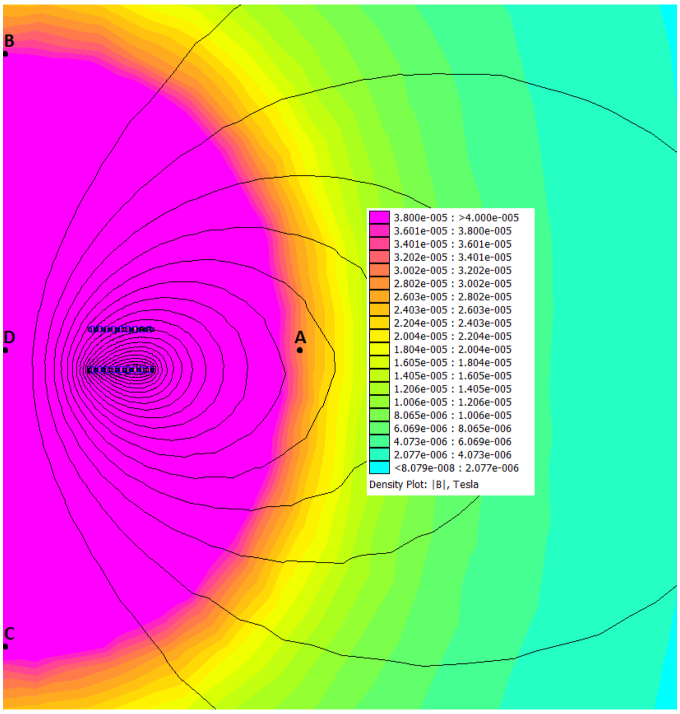

(b)

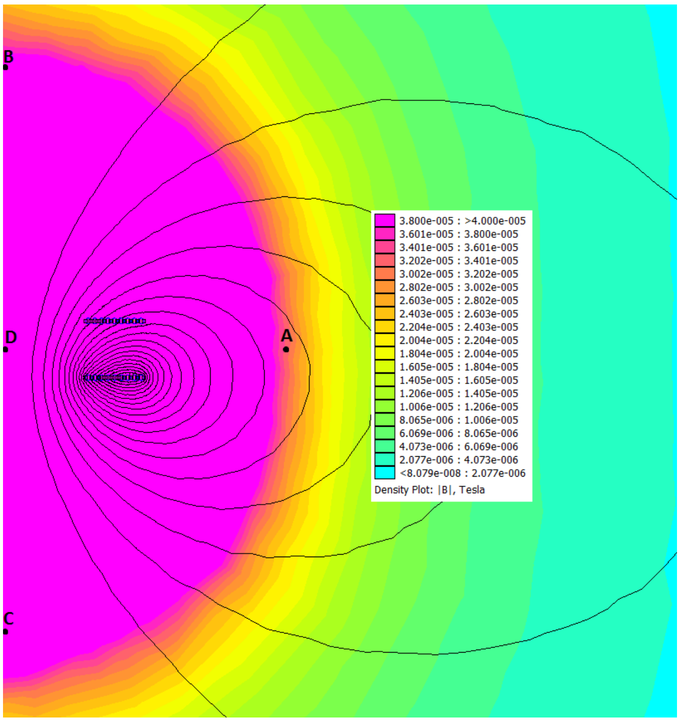

(c)

Fig. III.13. Magnetic flux density resulting from simulations:
(a) air gap = 1 cm; (b) air gap = 2 cm; (c ) air gap = 3 cm

According to the color key, the region where the magnitude of the magnetic flux density is higher than the ICNIRP limit of 38 µT corresponds to the first color starting from the top of the legend. Further from the coils, the magnetic field is lower. In Tab. III.4 nine points where the simulated magnetic flux density is equal to the ICNIRP limit are highlighted.

With reference to the figures, for each value of air gap the distances from the center of the system are given for the following directions: right, up, down.

In Tab. III.5, the value of the simulated magnetic flux density is given for each of the four points A, B, C and D, as higlighted in the figures. Each of A, B and C corresponds to a distance of 15 cm from the center D for each of the three directions.

**TABLE III.4.**

POINTS WHERE SIMULATED |B| = 38 μT

| Air gap | Distance from the center [cm] | | |
|---|---|---|---|
| | *right* | *up* | *down* |
| **1 cm** | 13.4 | 14.2 | 14.5 |
| **2 cm** | 13.8 | 14.6 | 15.4 |
| **3 cm** | 14.3 | 15.7 | 17.5 |

**TABLE III.5.**

SIMULATED |B| AT 4 DIFFERENT POINTS

| Air gap | \|B \|[μT] | | | |
|---|---|---|---|---|
| | *A* | *B* | *C* | *D* |
| **1 cm** | 25.5 | 32.3 | 35.2 | 654 |
| **2 cm** | 29.7 | 32 | 42.7 | 741 |
| **3 cm** | 33 | 42.7 | 57 | 807.5 |

As shown by the tabs, at 20 cm from the center of the system the simulated magnetic field, for a 100 W load power, is compliant with the guidelines of ICNIRP.

### III.5.1.2. Magnetic measurements

Fig. III.14 shows a 3D model of the coils. The three Cartesian axes are highlighted in order to give a reference concerning the points where the measurements have been actually taken.

In Tab. III.6 the values of magnetic flux density, arising from the experimental measurements, are provided.

With reference to Fig. III.14, the points of measurements are on the axes passing through the center (0,0,0). For example, with an air gap of 1 cm, at 15 cm from the center on the x axis, the measured |B| is 21.4 μT. In parentheses the corresponding points in the magnetic simulations are given, if existing.

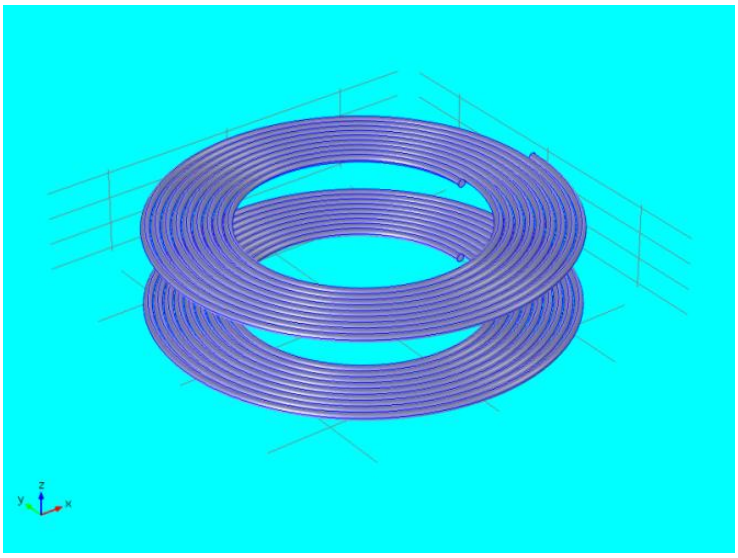

Fig. III.14. A 3D model of the proposed coils

**TABLE III.6.**

MEASURED |B| AT DIFFERENT POINTS

| **Air gap** | **\|B \|[µT]** | | | | | |
|---|---|---|---|---|---|---|
| | **x [cm]** | **y [cm]** | | **z [cm]** | | **(x,y,z)** |
| | ***15*** | ***-15*** | ***15 (A)*** | ***-15 (B)*** | ***15 (C)*** | ***(0,0,0) (D)*** |
| **1 cm** | 21.4 | 34.6 | 33.4 | 45.1 | 55.5 | 169.5 |
| **2 cm** | 35.4 | 50 | 31.9 | 63.7 | 74.8 | 942.3 |
| **3 cm** | 31.9 | 40.2 | 40.2 | 61.5 | 70.7 | 1021.4 |

As shown by the table, most of the points featuring values higher than the limit of 38 µT belong to the z axis. This reflects the data collected in Tab. III.4, where the *up* and *down* points show the highest values of distance, and in Tab. III.5, where the corresponding points B and C feature the highest values of magnetic flux density. Apart from the point D, which is not of concern for the goal of this paper, the difference between the experimental and the simulation data is in the range (20-30)%, which is acceptable considering the not perfect simulation model of the system and all the unavoidable sources of uncertainty of measurement. Therefore, a safety distance of 25 cm from the center is suggested for the proposed system.

In this Chapter a detailed description of the assembled IPT system has been provided and the experimental results have been discussed. For a 96 W power level, the coupling efficiency is 79%.

After the report of the results in terms of coupling and overall efficiency for different operation conditions, a magnetic characterization of the system has been carried out, through magnetic simulations and measurements.

If the center of the proposed IPT system placed upon the E-bike wheel is considered, a minimum 25 cm safety distance is suggested in order to respect the ICNIRP guidelines in terms of magnetic field exposure.

# Conclusions

This thesis has dealt with Wireless Charging Systems for Electric Vehicle Batteries.

An Inductive Power Transfer (IPT) system for an E-bike battery charging has been designed and assembled. The target is a 36 V 10 Ah $LiFePO_4$ battery and the power level ranges from 100 W to 250 W.

After the magnetic design of the IPT coils, the electric model of the coupling structure has been gained and acquired from an electronic simulation tool, in order to complete the design of the whole system.

A series-series (SS) compensation topology has been chosen for the capacitive network that has been connected to the coupled coils. In the assembled open-loop prototype, a half-bridge converter in the transmitter side and a four-diode rectifier in the receiver side have been designed.

From the experimental results, a 79 % coupling efficiency for an about 100 W level arises.

A magnetic characterization of the region surrounding the assembled prototype has been made as well. According to the magnetic field exposure guidelines, by ICNIRP, a minimum 25 cm distance from the center of the system is suggested as safety distance.

After the experimental measurements on the power efficiency, alternative solutions of power electronics and coupling structures have been investigated.

A Bi-Directional IPT system has been analyzed and an algorithm for its efficiency optimization has been proposed. Mathematical analysis has been validated through power electronics simulations.

For this system, an investigation has been carried out on different magnetic coupling structures, all compliant with an E-bike wheel, and the best option in terms of system efficiency and tolerance to lateral misalignments has been defined. The investigation has been made according to the results of 3D magnetic simulations and their elaboration.

The work of this thesis has been published in [118–121], [127–129], [137].

# References

[1] [Online]: http://home.howstuffworks.com/question292.htm.

[2] V. Boscaino, F. Pellitteri, L. R. R., and C. G., “Wireless battery chargers for portable applications: design and test of a high-efficiency power receiver,” *IET Power Electronics*, vol. 6, pp. 20–29, 2013.

[3] S. Segan. (2015) First Look at Intel’s Laptop Wireless Charging. [Online]. Available: http://www.pcmag.com/article2/0,2817,2490600,00.asp.

[4] [Online]: http://www.wirelesspowersupply.net/tv-that-uses-wireless-power-system.

[5] H. Z. Z. Beh, G. A. Covic, and J. T. Boys, “Wireless Fleet Charging System for Electric Bicycles,” *Emerging and Selected Topics in Power Electronics, IEEE Journal of*, vol. 3, no. 1, pp. 75–86, Mar. 2015.

[6] S. Asheer, A. Al-Marawani, T. Khattab, and A. Massoud, “Inductive power transfer with wireless communication system for electric vehicles,” in *GCC Conference and Exhibition (GCC), 2013 7th IEEE*, 2013, pp. 517–522.

[7] G. Jung, B. Song, S. Shin, S. Lee, J. Shin, Y. Kim, C. Lee, and S. Jung, “Wireless charging system for On-Line Electric Bus(OLEB) with series-connected road-embedded segment,” in *Environment and Electrical Engineering (EEEIC), 2013 12th International Conference on*, 2013, pp. 485–488.

[8] Y. Shi, L. Xie, Y. T. Hou, and H. D. Sherali, “On renewable sensor networks with wireless energy transfer,” in *INFOCOM, 2011 Proceedings IEEE*, 2011, pp. 1350–1358.

[9] J. Li, P. Li, H. Liu, D. Li, and J. Tang, “A contactless battery charging and monitoring system for wireless sensor network nodes,” in *Computer Science and Network Technology (ICCSNT), 2011 International Conference on*, 2011, vol. 3, pp. 1923–1926.

[10] L. Xie, Y. Shi, Y. T. Hou, W. Lou, H. D. Sherali, H. Zhou, and S. F. Midkiff, “A Mobile Platform for Wireless Charging and Data Collection in Sensor Networks,” *Selected Areas in Communications, IEEE Journal on*, vol. 33, no. 8, pp. 1521–1533, Aug. 2015.

[11] R. W. Porto, V. J. Brusamarello, I. Muller, and F. R. de Sousa, “Design and characterization of a power transfer inductive link for wireless sensor network nodes,” in *Instrumentation and Measurement Technology Conference (I2MTC), 2015 IEEE International*, 2015, pp. 1261–1266.

[12] C. Park and P. H. Chou, “AmbiMax: Autonomous Energy Harvesting Platform for Multi-Supply Wireless Sensor Nodes,” in *Sensor and Ad Hoc Communications and Networks, 2006. SECON ’06. 2006 3rd Annual IEEE Communications Society on*, 2006, vol. 1, pp. 168–177.

[13] F. I. Simjee and P. H. Chou, “Efficient Charging of Supercapacitors for Extended Lifetime of Wireless Sensor Nodes,” *Power Electronics, IEEE Transactions on*, vol. 23, no. 3, pp. 1526–1536, May 2008.

[14] Y. Yu, H. Hao, W. Wang, and L. Li, “Simulative and experimental research on wireless power transmission technique in implantable medical device,” in *Engineering in Medicine and Biology Society, 2009. EMBC 2009. Annual International Conference of the IEEE*, 2009, pp. 923–926.

[15] A. Pandey, F. Allos, A. P. Hu, and D. Budgett, “Integration of supercapacitors into wirelessly charged biomedical sensors,” in *Industrial Electronics and Applications (ICIEA), 2011 6th IEEE Conference on*, 2011, pp. 56–61.

[16] Q. Xu, H. Wang, Z. Gao, Z.-H. Mao, J. He, and M. Sun, “A Novel Mat-Based System for Position-Varying Wireless Power Transfer to Biomedical Implants,” *Magnetics, IEEE Transactions on*, vol. 49, no. 8, pp. 4774–4779, Aug. 2013.

[17] S. C. Nambiar and M. Manteghi, “A simple wireless power transfer scheme for implanted devices,” in *Radio Science Meeting (USNC-URSI NRSM), 2014 United States National Committee of URSI National*, 2014, pp. 1–1.

[18] P. Aqueveque and J. Barboza, “Wireless power system for charge supercapacitors as power sources for implantable devices,” in *Emerging Technologies: Wireless Power (WoW), 2015 IEEE PELS Workshop on*, 2015, pp. 1–5.

[19] S. Y. Hui, “Planar Wireless Charging Technology for Portable Electronic Products and Qi,” *Proceedings of the IEEE*, vol. 101, no. 6, pp. 1290–1301, Jun. 2013.

[20] [Online]: http://www.wirelesspowerconsortium.com/.

[21] [Online]: https://www.powermat.com/.

[22] F. Pellitteri, V. Boscaino, R. L. Rosa, and G. Capponi, “Improving the efficiency of a standard compliant wireless battery charger,” in *Universities Power Engineering Conference (UPEC), 2012 47th International*, 2012, pp. 1–6.

[23] V. Boscaino, F. Pellitteri, G. Capponi, and R. L. Rosa, “A wireless battery charger architecture for consumer electronics,” in *Consumer Electronics - Berlin (ICCE-Berlin), 2012 IEEE International Conference on*, 2012, pp. 84–88.

[24] D. Kurschner, C. Rathge, and U. Jumar, “Design Methodology for High Efficient Inductive Power Transfer Systems With High Coil Positioning Flexibility,” *Industrial Electronics, IEEE Transactions on*, vol. 60, no. 1, pp. 372–381, Jan. 2013.

[25] J. G. Taiber (2014). Advances in wireless charging of electrified vehicles and need for standardization. [Online]. Available: http://sites.ieee.org/isgt2014/files/2014/03/Day3_Panel3B2_Taiber.pdf.

[26] H. Z. Z. Beh, G. A. Covic, and J. T. Boys, “Investigation of Magnetic Couplers in Bicycle Kickstands for Wireless Charging of Electric Bicycles,” *Emerging and Selected Topics in Power Electronics, IEEE Journal of*, vol. 3, no. 1, pp. 87–100, Mar. 2015.

[27] H. Z. Z. Beh, G. A. Covic, and J. T. Boys, “Magnetic couplers in kickstands for wireless charging of electric bicycles,” in *Applied Power Electronics*

*Conference and Exposition (APEC), 2014 Twenty-Ninth Annual IEEE*, 2014, pp. 1348–1355.

[28] J.-I. Itoh, K. Noguchi, and K. Orikawa, “System design of electric assisted bicycle using EDLCs and wireless charger,” in *Power Electronics Conference (IPEC-Hiroshima 2014 - ECCE-ASIA), 2014 International*, 2014, pp. 2277–2284.

[29] RRC. (2014) RRC wireless power. [Online]. Available: http://www.rrc-wireless-power.com/fileadmin/website_wireless_power/Dokumente/News/Pressemitteilung_RRC_wireless_emobility_EN_021110.pdf.

[30] SEW EURODRIVE (2013) Taking mobility to the next level. [Online]. Available: http://www.sew-eurodrive.be/marketing/17058414.pdf.

[31] [Online]: http://www.slashgear.com/.

[32] R. Merritt (2010) Car makers signal interest in wireless charging. [Online]. Available: http://www.eetimes.com/document.asp?doc_id=1257680.

[33] [ONLINE]: http://evobsession.com/nissan-moving-ahead-higher-power-inductive-charging/.

[34] [Online]: https://www.pluglesspower.com/look/.

[35] [Online]: https://www.qualcomm.com/products/halo.

[36] [Online]: http://evobsession.com/wireless-ev-charging-as-fast-efficient-as-a-tesla-supercharger/.

[37] S. Raabe, G. A. Covic, J. T. Boys, C. Pennalligen, and P. Shekar, “Practical considerations in the design of multiphase pick-ups for contactless power transfer systems,” in *Industrial Electronics, 2009. IECON ’09. 35th Annual Conference of IEEE*, 2009, pp. 753–758.

[38] T. C. Y. Ho, B. Gomersall, and L. Ran, “Contactless charging for electric vehicles with a large air gap,” in *Power Electronics and Applications (EPE 2011), Proceedings of the 2011-14th European Conference on*, 2011, pp. 1–10.

[39] T. Yasuda, I. Norigoe, S. Abe, and Y. Kaneko, “Contactless charging systems,” in *Telecommunications Energy Conference (INTELEC), 2011 IEEE 33rd International*, 2011, pp. 1–7.

[40] Y. J. Jang, Y. D. Ko, and S. Jeong, “Optimal design of the wireless charging electric vehicle,” in *Electric Vehicle Conference (IEVC), 2012 IEEE International*, 2012, pp. 1–5.

[41] H. Takanashi, Y. Sato, Y. Kaneko, S. Abe, and T. Yasuda, “A large air gap 3 kW wireless power transfer system for electric vehicles,” in *Energy Conversion Congress and Exposition (ECCE), 2012 IEEE*, 2012, pp. 269–274.

[42] A. O. Di Tommaso, F. Genduso, and R. Miceli, “A small power transmission prototype for electric vehicle wireless battery charge applications,” in *Renewable Energy Research and Applications (ICRERA), 2012 International Conference on*, 2012, pp. 1–6.

[43] C.-Y. Huang, J. E. James, and G. A. Covic, “Design Considerations for Variable Coupling Lumped Coil Systems,” *Power Electronics, IEEE Transactions on*, vol. 30, no. 2, pp. 680–689, Feb. 2015.

[44] R. A. Deshmukh and D. B. Talange, “Design of 1kW inductive power transfer system for electric vehicle,” in *Advancements in Power and Energy (TAP Energy), 2015 International Conference on*, 2015, pp. 93–97.

[45] G. A. Covic, M. L. G. Kissin, D. Kacprzak, N. Clausen, and H. Hao, “A bipolar primary pad topology for EV stationary charging and highway power by inductive coupling,” in *Energy Conversion Congress and Exposition (ECCE), 2011 IEEE*, 2011, pp. 1832–1838.

[46] J. Huh, S. Lee, C. Park, G.-H. Cho, and C.-T. Rim, “High performance inductive power transfer system with narrow rail width for On-Line Electric Vehicles,” in *Energy Conversion Congress and Exposition (ECCE), 2010 IEEE*, 2010, pp. 647–651.

[47] S. Mohrehkesh and T. Nadeem, “Toward a wireless charging for battery electric vehicles at traffic intersections,” in *Intelligent Transportation Systems (ITSC), 2011 14th International IEEE Conference on*, 2011, pp. 113–118.

[48] S. Chopra and P. Bauer, “Driving Range Extension of EV With On-Road Contactless Power Transfer #x2014;A Case Study,” *Industrial Electronics, IEEE Transactions on*, vol. 60, no. 1, pp. 329–338, Jan. 2013.

[49] S. Chopra and P. Bauer, “On-road contactless power transfer - case study for driving range extension of EV,” in *IECON 2011 - 37th Annual Conference on IEEE Industrial Electronics Society*, 2011, pp. 4596–4602.

[50] J. G. Bolger, L. S. Ng, D. B. Turner, and R. I. Wallace, “Testing a prototype inductive power coupling for an electric highway system,” in *Vehicular Technology Conference, 1979. 29th IEEE*, 1979, vol. 29, pp. 48–56.

[51] U. K. Madawala, M. Neath, and D. J. Thrimawithana, “A Power Frequency Controller for Bidirectional Inductive Power Transfer Systems,” *Industrial Electronics, IEEE Transactions on*, vol. 60, no. 1, pp. 310–317, Jan. 2013.

[52] U. K. Madawala, M. J. Neath, and D. J. Thrimawithana, “The impact of variations in component values on power-frequency control of bi-directional Inductive Power Transfer systems,” in *Industrial Electronics (ISIE), 2012 IEEE International Symposium on*, 2012, pp. 560–565.

[53] U. K. Madawala and D. J. Thrimawithana, “A Bidirectional Inductive Power Interface for Electric Vehicles in V2G Systems,” *Industrial Electronics, IEEE Transactions on*, vol. 58, no. 10, pp. 4789–4796, Oct. 2011.

[54] U. K. Madawala and D. J. Thrimawithana, “Current sourced bi-directional inductive power transfer system,” *Power Electronics, IET*, vol. 4, no. 4, pp. 471–480, Apr. 2011.

[55] M. J. Neath, U. K. Madawala, and D. J. Thrimawithana, “A new controller for bi-directional inductive power transfer systems,” in *Industrial Electronics (ISIE), 2011 IEEE International Symposium on*, 2011, pp. 1951–1956.

[56] D. J. Thrimawithana, U. K. Madawala, and M. Neath, “A steady-state analysis of bi-directional inductive power transfer systems,” in *Industrial Technology (ICIT), 2013 IEEE International Conference on*, 2013, pp. 1618–1623.

[57] D. J. Thrimawithana, U. K. Madawala, and Y. Shi, “Design of a bi-directional inverter for a wireless V2G system,” in *Sustainable Energy Technologies (ICSET), 2010 IEEE International Conference on*, 2010, pp. 1–5.

[58] X. Xie, K. Zhou, L. Gao, X. Dai, Z.-H. Wang, and J. Gao, “Study on dynamical control of bi-directional Inductive Power Transfer system,” in *Industrial Electronics and Applications (ICIEA), 2013 8th IEEE Conference on*, 2013, pp. 1244–1247.

[59] “A. Brecher, D. Arthur, (2014) Review and Evaluation of Wireless Power Transfer (WPT) for Electric Transit Applications. [Online]. Available: http://www.fta.dot.gov/documents/FTA_Report_No._0060.pdf.” .

[60] M. Li, Q. Chen, J. Hou, W. Chen, and X. Ruan, “8-Type contactless transformer applied in railway inductive power transfer system,” in *Energy Conversion Congress and Exposition (ECCE), 2013 IEEE*, 2013, pp. 2233–2238.

[61] S. B. Lee, S. Ahn, J. H. Lee, and I. G. Jang, “Optimization of the wireless power transfer system in an electric railway,” in *Wireless Power Transfer Conference (WPTC), 2014 IEEE*, 2014, pp. 158–161.

[62] [Online]: http://primove.bombardier.com/.

[63] ThyssenKrupp. (2007) Inductive Power Supply (IPS®) for the Transrapid. [Online]. Available: http://www.maglev.ir/eng/documents/papers/conferences/maglev2006/topic5/IMT_CP_M2006_T5_1.pdf.

[64] W. Zhang, S.-C. Wong, C. K. Tse, and Q. Chen, “Analysis and Comparison of Secondary Series- and Parallel-Compensated Inductive Power Transfer Systems Operating for Optimal Efficiency and Load-Independent Voltage-Transfer Ratio,” *Power Electronics, IEEE Transactions on*, vol. 29, no. 6, pp. 2979–2990, Jun. 2014.

[65] I. Nam, R. Dougal, and E. Santi, “Optimal design method to achieve both good robustness and efficiency in loosely-coupled wireless charging system employing series-parallel resonant tank with asymmetrical magnetic coupler,” in *Energy Conversion Congress and Exposition (ECCE), 2013 IEEE*, 2013, pp. 3266–3276.

[66] I. Nam, R. Dougal, and E. Santi, “General optimal design method for series-series resonant tank in loosely-coupled wireless power transfer applications,” in *Applied Power Electronics Conference and Exposition (APEC), 2014 Twenty-Ninth Annual IEEE*, 2014, pp. 857–866.

[67] Y. Liao and X. Yuan, “Compensation topology for flat spiral coil inductive power transfer systems,” *Power Electronics, IET*, vol. 8, no. 10, pp. 1893–1901, 2015.

[68] Y. Liu, P. A. Hu, and U. K. Madawala, “Maximum power transfer and efficiency analysis of different inductive power transfer tuning topologies,” in *Industrial Electronics and Applications (ICIEA), 2015 IEEE 10th Conference on*, 2015, pp. 649–654.

[69] O. H. Stielau and G. A. Covic, “Design of loosely coupled inductive power transfer systems,” in *Power System Technology, 2000. Proceedings. PowerCon 2000. International Conference on*, 2000, vol. 1, pp. 85–90 vol.1.

[70] S. Chopra, “CONTACTLESS POWER TRANSFER FOR ELECTRIC VEHICLE CHARGING APPLICATION,” Delft University of Technology, the Netherlands, 2011.

[71] T. Diekhans and R. W. De Doncker, “A dual-side controlled inductive power transfer system optimized for large coupling factor variations,” in *Energy Conversion Congress and Exposition (ECCE), 2014 IEEE*, 2014, pp. 652–659.

[72] T. Diekhans, F. Stewing, G. Engelmann, H. van Hoek, and R. W. De Doncker, “A systematic comparison of hard- and soft-switching topologies for inductive power transfer systems,” in *Electric Drives Production Conference (EDPC), 2014 4th International*, 2014, pp. 1–8.

[73] U. K. Madawala and D. J. Thrimawithana, “A ring inductive power transfer system,” in *Industrial Technology (ICIT), 2010 IEEE International Conference on*, 2010, pp. 667–672.

[74] S. Buller, M. Thele, R. W. De Doncker, and E. Karden, “Supercapacitors and lithium-ion batteries for power electronic applications,” *Industry Applications Magazine, IEEE*, vol. 11, no. 2, pp. 62–67, Mar. 2005.

[75] H. Han, H. Xu, Z. Yuan, and Y. Zhao, “Modeling for lithium-ion battery used in electric vehicles,” in *Transportation Electrification Asia-Pacific (ITEC Asia-Pacific), 2014 IEEE Conference and Expo*, 2014, pp. 1–5.

[76] G. C. Bruce and L. Marcoux, “Large lithium ion batteries for aerospace and aircraft applications,” *Aerospace and Electronic Systems Magazine, IEEE*, vol. 16, no. 9, pp. 24–28, Sep. 2001.

[77] A.-I. Stan, M. Swierczynski, D.-I. Stroe, R. Teodorescu, and S. J. Andreasen, “Lithium ion battery chemistries from renewable energy storage to automotive and back-up power applications #x2014; An overview,” in *Optimization of Electrical and Electronic Equipment (OPTIM), 2014 International Conference on*, 2014, pp. 713–720.

[78] L. W. Yao and J. A. Aziz, “High capacity lifepo4 battery model with consideration of nonlinear capacity effects,” in *Power Electronics and Motion Control Conference (IPEMC), 2012 7th International*, 2012, vol. 1, pp. 182–187.

[79] L. Gao, S. Liu, and R. A. Dougal, “Dynamic lithium-ion battery model for system simulation,” *Components and Packaging Technologies, IEEE Transactions on*, vol. 25, no. 3, pp. 495–505, Sep. 2002.

[80] M. Chen and G. A. Rincon-Mora, “Accurate electrical battery model capable of predicting runtime and I-V performance,” *Energy Conversion, IEEE Transactions on*, vol. 21, no. 2, pp. 504–511, Jun. 2006.

[81] E. Kamal, A. El Hajjaji, and A. M. Mabwe, “State of charge estimation based on extened Kalman filter algorithm for Lithium-Ion battery,” in *Control and*

*Automation (MED), 2015 23th Mediterranean Conference on*, 2015, pp. 734–739.

[82] Z. Zhu, J. Sun, and D. Liu, “Online state of charge EKF estimation for LiFePO4 battery management systems,” in *Intelligent Signal Processing and Communications Systems (ISPACS), 2012 International Symposium on*, 2012, pp. 609–614.

[83] S. Y. R. Hui, W. Zhong, and C. K. Lee, “A Critical Review of Recent Progress in Mid-Range Wireless Power Transfer,” *Power Electronics, IEEE Transactions on*, vol. 29, no. 9, pp. 4500–4511, 2014.

[84] F. Musavi and W. Eberle, “Overview of wireless power transfer technologies for electric vehicle battery charging,” *Power Electronics, IET*, vol. 7, no. 1, pp. 60–66, Jan. 2014.

[85] T. Imura and Y. Hori, “Maximizing Air Gap and Efficiency of Magnetic Resonant Coupling for Wireless Power Transfer Using Equivalent Circuit and Neumann Formula,” *Industrial Electronics, IEEE Transactions on*, vol. 58, no. 10, pp. 4746–4752, Oct. 2011.

[86] S. Valtchev, B. Borges, K. Brandisky, and J. B. Klaassens, “Resonant Contactless Energy Transfer With Improved Efficiency,” *Power Electronics, IEEE Transactions on*, vol. 24, no. 3, pp. 685–699, Mar. 2009.

[87] S. Kong, M. Kim, K. Koo, S. Ahn, B. Bae, and J. Kim, “Analytical expressions for maximum transferred power in wireless power transfer systems,” in *Electromagnetic Compatibility (EMC), 2011 IEEE International Symposium on*, 2011, pp. 379–383.

[88] Y. Moriwaki, T. Imura, and Y. Hori, “Basic study on reduction of reflected power using DC/DC converters in wireless power transfer system via magnetic resonant coupling,” in *Telecommunications Energy Conference (INTELEC), 2011 IEEE 33rd International*, 2011, pp. 1–5.

[89] N. Inagaki, “Theory of Image Impedance Matching for Inductively Coupled Power Transfer Systems,” *Microwave Theory and Techniques, IEEE Transactions on*, vol. 62, no. 4, pp. 901–908, Apr. 2014.

[90] C.-S. Wang, G. A. Covic, and O. H. Stielau, “Power transfer capability and bifurcation phenomena of loosely coupled inductive power transfer systems,” *Industrial Electronics, IEEE Transactions on*, vol. 51, no. 1, pp. 148–157, 2004.

[91] F. Aming, Q. Haihong, M. Zhixin, and P. Pingyan, “Analysis of Bifurcation Phenomena Based on Optimized Transformer in Loosely Coupled Inductive Power Transfer System,” in *Electrical and Control Engineering (ICECE), 2010 International Conference on*, 2010, pp. 3324–3327.

[92] C.-S. Wang, G. A. Covic, and O. H. Stielau, “General stability criterions for zero phase angle controlled loosely coupled inductive power transfer systems,” in *Industrial Electronics Society, 2001. IECON ’01. The 27th Annual Conference of the IEEE*, 2001, vol. 2, pp. 1049–1054 vol.2.

[93] C.-B. Park and H.-W. Lee, “Study on the Optimal Switching Frequency for Maximum Wireless Power Transfer in a Variable Airgap System,” *Emerging and Selected Topics in Power Electronics, IEEE Journal of*, vol. 3, no. 1, pp. 201–204, Mar. 2015.

[94] M. Budhia, G. A. Covic, and J. T. Boys, “Design and Optimization of Circular Magnetic Structures for Lumped Inductive Power Transfer Systems,” *Power Electronics, IEEE Transactions on*, vol. 26, no. 11, pp. 3096–3108, Nov. 2011.

[95] M. Budhia, G. A. Covic, and J. T. Boys, “Design and optimisation of magnetic structures for lumped Inductive Power Transfer systems,” in *Energy Conversion Congress and Exposition, 2009. ECCE 2009. IEEE*, 2009, pp. 2081–2088.

[96] Y. Nagatsuka, N. Ehara, Y. Kaneko, S. Abe, and T. Yasuda, “Compact contactless power transfer system for electric vehicles,” in *Power Electronics Conference (IPEC), 2010 International*, 2010, pp. 807–813.

[97] M. Chigira, Y. Nagatsuka, Y. Kaneko, S. Abe, T. Yasuda, and A. Suzuki, “Small-size light-weight transformer with new core structure for contactless

electric vehicle power transfer system," in *Energy Conversion Congress and Exposition (ECCE), 2011 IEEE*, 2011, pp. 260–266.

[98] M. Budhia, J. T. Boys, G. A. Covic, and C.-Y. Huang, "Development of a Single-Sided Flux Magnetic Coupler for Electric Vehicle IPT Charging Systems," *Industrial Electronics, IEEE Transactions on*, vol. 60, no. 1, pp. 318–328, Jan. 2013.

[99] G. A. Covic and J. T. Boys, "Modern Trends in Inductive Power Transfer for Transportation Applications," *Emerging and Selected Topics in Power Electronics, IEEE Journal of*, vol. 1, no. 1, pp. 28–41, Mar. 2013.

[100] G. R. Nagendra, G. A. Covic, and J. T. Boys, "Determining the Physical Size of Inductive Couplers for IPT EV Systems," *Emerging and Selected Topics in Power Electronics, IEEE Journal of*, vol. 2, no. 3, pp. 571–583, 2014.

[101] S. Hasanzadeh, S. Vaez-Zadeh, and A. H. Isfahani, "Optimization of a Contactless Power Transfer System for Electric Vehicles," *Vehicular Technology, IEEE Transactions on*, vol. 61, no. 8, pp. 3566–3573, 2012.

[102] J. Sallan, J. L. Villa, A. Llombart, and J. F. Sanz, "Optimal Design of ICPT Systems Applied to Electric Vehicle Battery Charge," *Industrial Electronics, IEEE Transactions on*, vol. 56, no. 6, pp. 2140–2149, 2009.

[103] P. Ning, O. Onar, and J. Miller, "Genetic algorithm based coil system optimization for wireless power charging of electric vehicles," in *Transportation Electrification Conference and Expo (ITEC), 2013 IEEE*, 2013, pp. 1–5.

[104] J. T. Boys, G. A. Covic, and A. W. Green, "Stability and control of inductively coupled power transfer systems," *Electric Power Applications, IEE Proceedings* -, vol. 147, no. 1, pp. 37–43, Jan. 2000.

[105] R. Bosshard, U. Badstubner, J. W. Kolar, and I. Stevanovic, "Comparative evaluation of control methods for Inductive Power Transfer," in *Renewable Energy Research and Applications (ICRERA), 2012 International Conference on*, 2012, pp. 1–6.

[106] W. P. Choi, W. C. Ho, X. Liu, and S. Y. R. Hui, “Comparative study on power conversion methods for wireless battery charging platform,” in *Power Electronics and Motion Control Conference (EPE/PEMC), 2010 14th International*, 2010, pp. S15–9–S15–16.

[107] U. K. Madawala and D. J. Thrimawithana, “A two-way inductive power interface for single loads,” in *Industrial Technology (ICIT), 2010 IEEE International Conference on*, 2010, pp. 673–678.

[108] C. Zhao, Z. Wang, J. Du, J. Wu, S. Zong, and X. He, “Active resonance wireless power transfer system using phase shift control strategy,” in *Applied Power Electronics Conference and Exposition (APEC), 2014 Twenty-Ninth Annual IEEE*, 2014, pp. 1336–1341.

[109] U. K. Madawala and D. J. Thrimawithana, “A single controller for inductive power transfer systems,” in *Industrial Electronics, 2009. IECON ’09. 35th Annual Conference of IEEE*, 2009, pp. 109–113.

[110] D. J. Thrimawithana and U. K. Madawala, “A primary side controller for inductive power transfer systems,” in *Industrial Technology (ICIT), 2010 IEEE International Conference on*, 2010, pp. 661–666.

[111] U. K. Madawala and D. J. Thrimawithana, “New technique for inductive power transfer using a single controller,” *Power Electronics, IET*, vol. 5, no. 2, pp. 248–256, Feb. 2012.

[112] H. Jiang, P. Brazis, M. Tabaddor, and J. Bablo, “Safety considerations of wireless charger for electric vehicles #x2014; A review paper,” in *Product Compliance Engineering (ISPCE), 2012 IEEE Symposium on*, 2012, pp. 1–6.

[113] [Online]: http://news.bbc.co.uk/2/hi/technology/6725955.stm.

[114] D. Schneider, ‘A Critical Look at Wireless Power’, IEEE Spectrum, May 2010.

[115] IEEE Standard C95.1, ‘IEEE Standard for Safety Levels with Respect to Human Exposure to Radio Frequency Electromagnetic Fields, 3 kHz to 300 GHz’, 2005.

[116] International Commission on Non-Ionizing Radiation Protection, ‘Guidelines for limiting exposure to time-varying electric and magnetic fields (1 Hz–100 kHz),’ Health Phys., vol. 99, no. 6, pp. 818–836, 2010.

[117] C.-Y. Huang, J. T. Boys, G. A. Covic, and M. Budhia, “Practical considerations for designing IPT system for EV battery charging,” in *Vehicle Power and Propulsion Conference, 2009. VPPC ’09. IEEE,* 2009, pp. 402–407.

[118] F. Pellitteri, V. Boscaino, A. O. Di Tommaso, F. Genduso, and R. Miceli, “E-bike battery charging: Methods and circuits,” in *Clean Electrical Power (ICCEP), 2013 International Conference on,* 2013, pp. 107–114.

[119] F. Pellitteri, V. Boscaino, A. O. Di Tommaso, R. Miceli, and G. Capponi, “Inductive Power Transfer for 100W battery charging,” in *Industrial Electronics Society, IECON 2013 - 39th Annual Conference of the IEEE,* 2013, pp. 894–899.

[120] F. Pellitteri, V. Boscaino, A. O. Di Tommaso, R. Miceli, and G. Capponi, “Wireless battery charging: E-bike application,” in *Renewable Energy Research and Applications (ICRERA), 2013 International Conference on,* 2013, pp. 247–251.

[121] F. Pellitteri, V. Boscaino, A. O. Di Tommaso, R. Miceli, and G. Capponi, “Experimental test on a Contactless Power Transfer system,” in *Ecological Vehicles and Renewable Energies (EVER), 2014 Ninth International Conference on,* 2014, pp. 1–6.

[122] X. Liu and S. Y. Hui, “Optimal Design of a Hybrid Winding Structure for Planar Contactless Battery Charging Platform,” in *Industry Applications Conference, 2006. 41st IAS Annual Meeting. Conference Record of the 2006 IEEE,* 2006, vol. 5, pp. 2568–2575.

[123] Z. N. Low, R. A. Chinga, R. Tseng, and J. Lin, “Design and Test of a High-Power High-Efficiency Loosely Coupled Planar Wireless Power Transfer System,” *Industrial Electronics, IEEE Transactions on,* vol. 56, no. 5, pp. 1801–1812, May 2009.

[124] Open Source Software ‘Finite Element Method Magnetics’, FEMM - Version 4.2, 2009.

[125] Sofwtare ‘Powersim Studio’, PSIM Studio – Version 9.1, Powersim Inc., 2012.

[126] Software ‘MATLAB Simulink’– Release 2012a, 2012, by MathWorks.

[127] F. Pellitteri, V. Boscaino, R. Miceli, and U. K. Madawala, “Power tracking with maximum efficiency for wireless charging of E-bikes,” in *Electric Vehicle Conference (IEVC), 2014 IEEE International*, 2014, pp. 1–7.

[128] F. Pellitteri, V. Boscaino, A. O. Di Tommaso, and R. Miceli, “Efficiency optimization in bi-directional inductive power transfer systems,” in *Electrical Systems for Aircraft, Railway, Ship Propulsion and Road Vehicles (ESARS), 2015 International Conference on*, 2015, pp. 1–6.

[129] F. Pellitteri, A. O. Di Tommaso, and R. Miceli, “Investigation of inductive coupling solutions for E-bike wireless charging,” in *Power Engineering Conference (UPEC), 2015 50th International Universities*, 2015, pp. 1–6.

[130] Software ‘COMSOL Multiphysics’ – Version 5.0, 2015, by COMSOL Inc.

[131] [Online]: http://en.tdk.eu/.

[132] Fairchild Semiconductor (2012). ‘FAN7390 Datasheet (PDF)’. [Online]. Available: https://www.fairchildsemi.com/datasheets/FA/FAN7390.pdf.

[133] STMicroelectronics, ‘STB120NF10T4 Datasheet (PDF)’, power MOSFET datasheet.

[134] [Online]: http://www.vishay.com/.

[135] [Online]: http://www.panasonic.com/it/.

[136] Software ‘Eagle’– v5.6.0, by CadSoft.

[137] F. Pellitteri, G. Ala, M. Caruso, S. Ganci, and R. Miceli, “Physiological compatibility of wireless chargers for electric bicycles,” in *Renewable Energy Research and Application (ICRERA), 2015 International Conference on*, 2015.